THESIS

DESIGN AND FABRICATION OF A 3-D PRINTABLE COUNTER-FLOW/PRECIPITATION

HEAT EXCHANGER FOR USE WITH A NOVEL OFF-GRID SOLID STATE

REFRIGERATION SYSTEM

Submitted by

Sean Thomas Ryan

Department of Mechanical Engineering

Master's Committee:

    Advisor: Anthony Marchese

    Allan Kirkpatrick
    Sybil Sharvelle

ABSTRACT

DESIGN AND FABRICATION OF A 3-D PRINTABLE COUNTER-FLOW/PRECIPITATION

HEAT EXCHANGER FOR USE WITH A NOVEL OFF-GRID SOLID STATE

REFRIGERATION SYSTEM

Off-grid refrigeration technologies are currently limited to either vapor-compression cycles driven by photovoltaics or solar thermal absorption cycles. Rebound Technologies has recently developed a novel off-grid refrigeration system called Sunchill^{TM} for agricultural applications in humid environments in the developing world. The Sunchill^{TM} refrigeration system utilizes the daily high and low temperatures to drive a 24 hour refrigeration cycle. Cooling is provided by the dissolution of an endothermic salt, sodium carbonate decahydrate. Once the salt is solvated and cooling is delivered to freshly harvest crops, the system is "recharged" in a multi-step process that relies on a solar collector, an air-gap membrane unit and a heat exchanger. The heat exchanger, which is the focus of this thesis, is required to remove 36.6 MJ of heat over a twelve hour period in order to "recharge" the system. The heat exchanger is also required to transfer heat from a fresh water stream to a cold brine solution to generate the cold water necessary to submerse and cool harvested crops. To provide a sustainable technology to the target community, the feasibility of fabricating the heat exchanger via the low cost 3-D printing method of fused filament fabrication (FFF) was examined. This thesis presents the design, development, and manufacturing considerations that were performed in support of developing a waterproof, counter-flow, 3-D printable heat exchanger. Initial geometries and performance were modeled by constructing a linear thermal resistance network with truncating temperatures of 30°C (saturated brine temperature) and 18°C (average daily low temperature). The required surface area of the heat exchanger was found to be

20.46 m^2 to remove the required 36.6 MJ of heat. Iterative print tests were conducted to arrive at the wall thickness, hexagon shape, and double wall structure of the heat exchanger. A laboratory-scale heat exchanger was fabricated using a Lulzbot Taz 4 printer from acrylonitrile butadiene styrene (ABS) polymer. Performance was verified empirically for the laboratory-scale unit. A heat transfer rate of 22.8 W was obtained at a flow rate of 0.00075 kg/s. The results of this thesis demonstrate the feasibility of manufacturing low cost heat exchangers using additive manufacturing techniques.

ACKNOWLEDGMENTS

TABLE OF CONTENTS

LIST OF TABLES

LIST OF FIGURES

LIST OF VARIABLES

ΔH_{solv} : Enthalpy of solvation of $Na_2CO_3 \cdot 10H_2O$

E_{req} : Energy required to provide farmer's cooling demand

m_{salt} : Mass of $Na_2CO_3 \cdot 10H_2O$ to provide specified cooling

m_{Na2CO3} : Mass of Na_2CO_3 in m_{salt}

m_{H2O} : Mass of H_2O in m_{salt}

$m_{specNa2CO3}$: Mass of Na_2CO_3 that remains in solution in all modes of system operation

$m_{specH2O}$: Mass of H_2O that remains in solution in all modes of system operation

$m_{solvH2O}$: Mass of H_2O necessary to dissolve m_{salt}

m_{PHX} : Mass of solution and/or precipitate contained in PHX during nighttime charge mode

m_{Total} : Total mass of Na_2CO_3 and H_2O in system

C_{high}: Initial concentration in PHX at the beginning of the nighttime charge mode

C_{low}: Final, saturation concentration of solution at low ambient temp during nighttime charge mode

$C_{dissolve}$: Concentration of solution at end of discharge/cooling mode

V_{PHX}: Volume of the brine chamber of the PHX

ρ_{Na2CO3}: Density of Na_2CO_3 in aqueous solution

C_{Na2CO3}: Concentration of Na_2CO_3 in aqueous solution

1   Introduction

Off-grid refrigeration technologies are currently limited to either vapor-compression cycles driven by photovoltaics or solar thermal absorption cycles.[1,2,3,4,5] Rebound Technologies has proposed an off-grid prechiller called Sunchill[TM] for developing-world agriculture that utilizes the daytime sun and nightly low temperature to drive a liquid-solid refrigeration cycle. A water based refrigerant does not have the problem of leakage that the high pressure vapor phase has in standard refrigerant cycles. Rebound's system also does not use pumps, compressors, solar trackers or any other moving part that tends to be the source of failure of other systems. The system is designed such that it can be built and maintained by the community, almost in its entirety, from locally sourced parts. An illustration of Rebound's refrigeration cycle can be seen in figure 1. Unlike a typical vapor compression refrigeration system, Sunchill[TM] does not provide cooling continuously. Instead, Sunchill[TM] provides the necessary cooling once a day in the morning and the remaining hours are used to recharge the system for the next cooling event.
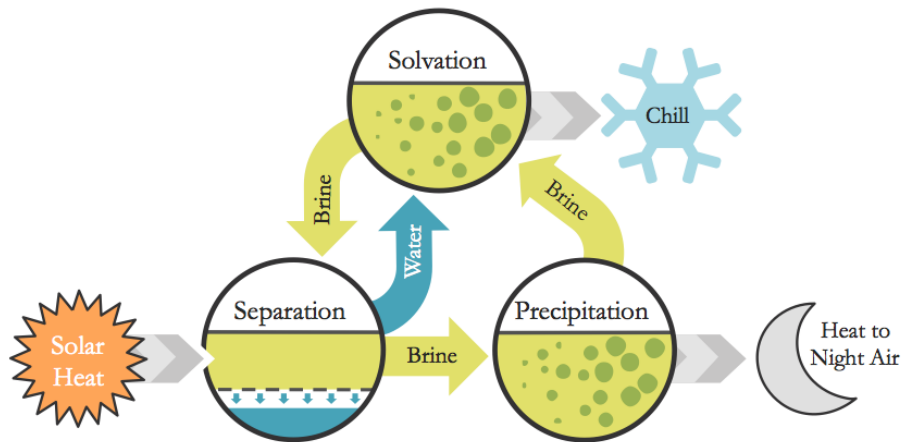
Figure 1. The four stages of the Rebound refrigeration cycle.

In order to remove the field heat of freshly harvested crops the farmer of Mozambique Organicos, Koos van de Merwe, requires two kilowatts of cooling from 10°C water over four hours in the morning. To accomplish this, the endothermic dissolution of a hydrated salt, sodium carbonate decahydrate ($Na_2CO_3 \cdot H_2O$) is utilized. Transfer of heat from ambient temperature water

to the cold brine solution via a heat exchanger will produce the required 10°C cooling water that harvested crops can then be submersed in. After solvation and cooling is complete, the brine is then concentrated using an air-gap membrane assembled by the Fraunhofer Institute. In order to recover the initial mass of salt that provided the cooling, one must remove the heat of the concentrating step as well as the heat of precipitation. This step is to be completed over night, utilizing the daily low temperature, and subsequently driving the heat transfer from the brine solution. To achieve this, a heat exchanger is required and it is proposed that this precipitation heat exchanger (PHX) be built using 3D printing methods.

It can be inferred that there are two distinct modes required of the PHX. The first is the precipitation step where heat is transferred from the hot brine solution to the low nighttime temperature surroundings. With no pumps in the system, this is to be done via natural convection. In the section that follows the required geometry/size of the part is discussed due to the constraint of natural convection driven heat exchange. This operation of the PHX will be referred to as the precipitation mode.

The second mode operates during the cooling step where a liquid to liquid heat exchange occurs from the ambient water stream to the solvating brine flow where both flow paths are gravity fed. It is necessary to keep the water that cools crops and brine solution separate, this leads to the necessity of a double-pipe (or double walled) heat exchanger to prevent mixing of the fluids. Two types of flow arrangements exist for a double-pipe heat exchanger, parallel flow and counter flow.[6,7,8] In parallel flow the hot fluid and cold fluid enter the heat exchanger on the same side and move together in the same direction, hence parallel flow. In counter flow the hot fluid and cold fluid enter on opposite sides of the heat exchanger and flow past one another in opposite directions.

In order to compare the use of heat exchangers it is convenient to use the logarithmic mean temperature difference, ΔT_{lm}. This establishes an equivalent mean temperature difference between the two fluids in the heat exchanger being considered. Taking the inlet and outlet temperatures of the cold fluid to be $T_{in,c}$ and $T_{out,c}$ and the inlet and outlet temperatures of the hot fluid to be $T_{in,h}$ and $T_{out,h}$ respectively, the log mean temperature difference of a heat exchanger can be found using equation 1. For a specified inlet temperature of the hot fluid and outlet temperature of the cold fluid, or vice versa, the log mean temperature difference for a counter-flow arrangement will be less than a parallel-flow arrangement.[7] Subsequently the required surface area of a counter-flow heat exchanger is less than that of a parallel-flow heat exchanger.

$$\Delta T_{lm} = \frac{\left(\left(T_{in,hot} - T_{in,cold}\right) - \left(T_{out,hot} - T_{out,cold}\right)\right)}{ln\left(\dfrac{\left(T_{in,hot} - T_{in,cold}\right)}{\left(T_{out,hot} - T_{out,cold}\right)}\right)} \quad (1)$$

Since surface area needs to be minimized with the PHX to minimize overall print time, material, and cost a counter-flow arrangement for the PHX was be adopted. The cooling step through the PHX will be referred to as the counter-flow mode.

3D printing for manufacturing the PHX is appealing in that it does not require the precise machining, expensive equipment, or skilled labor as metallic heat exchangers.[9] It is a cost effective technique and a printer could be provided with the refrigeration unit to initially build the PHX and to repair any of the 3D printed parts of the system. This manufacturing technique also allows for a design of the PHX that is not capable of being fabricated by standard machining. As mentioned, a double wall system is required to transfer heat between liquids during the cooling step. The final complex geometry and nesting of separate compartments of the PHX would be nearly impossible using metallic machining processes, thus the use of 3D printing allows for a greater breadth of

complexity in geometry and design while maintaining ease of fabrication. 3D printing also aids in

the goal for the project of providing a self-sustainable refrigeration unit. Any repairs to be done on

the system could be achieved by a local "handyman" with basic mechanical and plumbing

knowledge. This person could be quickly trained to use the 3D printer for repair of the PHX and

other printed system components as well as observe and aid in the initial system installation.

1.1 Developments in Plastic Heat Exchanger Technology

Plastic heat exchangers are often sought after due to their unique physical properties such as

flexibility, corrosion resistance, limited weight, and simplicity of manufacturing. In 1967, the first

plastic heat exchanger was produced by Dupont. The heat exchanger comprised of a plastic tube

bundle where each tube was made of thin walled PTFE or Teflon.[10] On each end of the bundle, a

manifold/clamp would secure the loose tube bundle into a tight honeycomb like structure. Due to

the fully fluorinated polymer that is PTFE, it is corrosion and reaction resistant.[11] For this reason,

the Dupont heat exchanger was often used to cool chemical baths and acids in a shell-and-tube

immersion configuration. However, PTFE is susceptible to defluorination by reaction with alkali

metals such as sodium.[12,13]

To combat the low thermal conductivity of plastics, the wall thickness of the Dupont flexible

tube heat exchanger was kept to 5-15% of the diameter of the tube. Diameters ranged from 2 mm

to 6 mm with tube arrays containing 7 to 5000 tubes. The surface area to volume ratio of these heat

exchangers ranged from 130-650 m^{-1} and overall heat transfer coefficients ranged from 34 W/m^2K

for air/gas heat exchangers to 560 W/m^2K for water/water heat exchangers[14].

In the late nineties Dupont and Magneti Marelli Climatizzazione S.p.A. worked to develop an

all-nylon charge air cooler for automotive applications[15]. By reducing wall thickness, a plastic air-

to-air heat exchanger could match the heat transfer characteristics of a standard aluminum charge

air cooler. The low thermal conductivity of plastic resins required the use of tubes only instead of the standard geometry of louvered fins connected to tubes. Additional surface area was achieved by closely spacing these tubes of small diameter and thin walls. The overall heat transfer coefficient for the all-nylon charge air cooler ranged between 10-18 W/m^{2}K corresponding to a range of cooling air mass flow rates of 0.1-0.4 kg/s. Although the heat transfer coefficients for the plastic heat exchanger were on average 15% higher than the standard aluminum charge air cooler, the pressure drop was on average 28% higher. In later automotive field tests, there was no noticeable difference in performance from the use of the all-nylon charge air cooler.

In 2004, Zaheed and Jachuck reviewed polymer film compact heat exchangers (PFCHE).[16] They described that a liquid-liquid heat exchanger utilizing 100 µm thick polymer films developed by the Process Intensification and Innovation Center (PIIS) at the University of Newcastle Upon Tyne could provide significantly better thermal performance from previous developments of polymer heat exchangers that typically had 0.5-1 mm wall thicknesses. Corrugation on the films enhanced the heat transfer as it aided in the mixing of the fluid flow (see figure 2). The thin polymer films were made from poly ether ether ketone (PEEK) for its chemical and fatigue resistance. PEEK also exhibits good thermal stability and is capable of a working temperature of 220 °C. Polymer film compact heat exchangers such as the corrugated heat exchanger previously described have applications in the desalination industry, for absorption chillers, and for solar collectors to name a few.
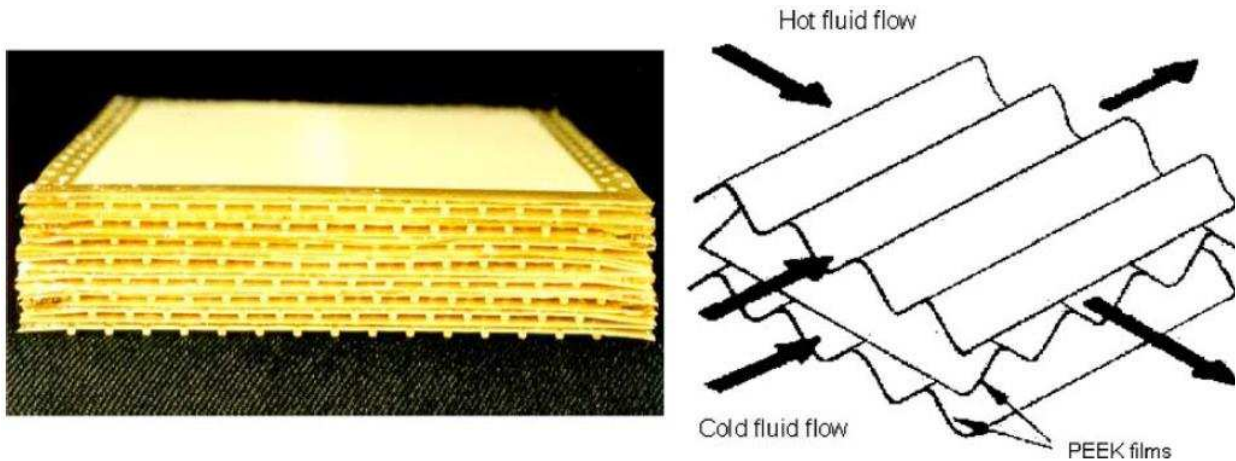
Figure 2. PEEK corrugated polymer film in compact heat exchanger.

Chen, Li, and Guo of Tsinghua University in Beijing investigated finned-tube air-water heat exchangers for use in liquid desiccant air conditioning, heat recovery, sea water desalination, water source heat pump, etc.[17] Modified types of polypropylene (PP) of differing crystalline unit cells were used with high thermal conductivities of 2.3 W/m⁻K (PP-α) and 16.5 W/m⁻K (PP-β). Unaltered polypropylene has a thermal conductivity of 0.2 W/m-K. The injection molded heat exchanger fin and tube wall thicknesses were on average, 0.6 mm and 0.4 mm respectively. Spacing between tubes was 2.8 cm. Overall heat transfer coefficients for PP, PP-α, PP-β variations of the heat exchanger were 8.94, 18.79, and 33.91 W/m²K respectively, at an air flow rate of 670 m³/h and water flow rate of 0.12 kg/s. The temperature of the incoming air was 26°C and the temperature of the incoming chilling water was 8°C. Chen et. Al. found that if the thermal conductivity for a plastic heat exchanger was greater than 15 W/m-K, it could reach 95% of the performance of a titanium heat exchanger and 84% of the performance of an aluminum or copper heat exchanger with the same dimensions and working conditions. They also determined that the thermal resistance of the walls was only the pinch point when the thermal conductivity is extremely

6

low, such as that of unaltered polypropylene. For highly conductive plastics, the dominant resistance is that of air.

Plastic heat exchangers offer a low weight, cost effective, corrosion resistant, and easily fabricated alternative to their metallic counterparts. While most plastic heat exchangers are injection molded, there are limited examples of heat exchangers manufactured by the relatively new and recently popular technique of 3D printing. In 2014, Juan Cevallos of the University of Maryland is said to have designed and built the first 3D printed heat exchanger.[18]
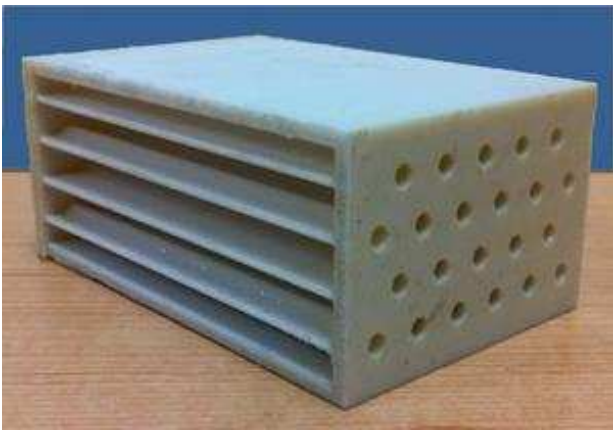
Figure 3. The WTHX developed by Juan Cevallos in collaboration with Statasys.[18]

In collaboration with Stratasys Inc., Cevallos successfully produced a "webbed tube heat exchanger (WTHX)" from a composite polymer matrix that was capable of removing 65W of heat from 120°C air flowing perpendicular to the WTHX with 27°C building water flowing into the heat exchanger. Cevallos's geometry for the WTHX was a stack of flat plates with an array of tubes spanning the length of each plate and had a thickness of 2 mm. The WTHX was comprised of a total of 4 plates where each plate-tube array was staggered from the last. On either end was a "webbed" manifold that water would flow at the building's temperature and pressure. The WTHX can be seen in figure 3.

1.2 Overview of Fused Filament Fabrication

Fused filament fabrication (FFF) is one of the fastest growing technologies of additive manufacturing.[19] Fused filament fabrication is known as a melt extrusion-based system and relies on seven basic principles to achieve a printed part. Those principles being the loading of material,

liquefaction of that material, material flow, extrusion, solidification, positional control, bonding, and support generation.[9]

For a FFF machine, material is typically loaded with a filament. This filament is provided on a spool which allows for a "continuous" flow of material as the filament is fed into the extrusion head. The feeding of the filament acts as a source of pressure for the nozzle in order for extrusion to take place.

Extrusion based systems operate on the basis that the feed material can be heated in such a manner as to liquefy and that liquid can be forced through a nozzle to be deposited on the build plate surface (Figure 4). The temperature for the heating element is set to be greater than the glass transition temperature but remain below the melting point of the feed material. For the most common polymer filament, acrylonitrile butadiene styrene (ABS), the glass transition temperature is 105°C.[20] Due to the amorphous nature of ABS, it does not have a true melting point but extrusion head temperature is set to 230°C.
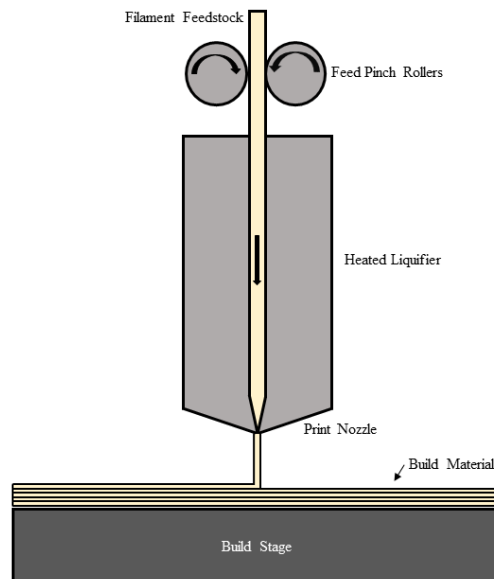
Figure 4. Schematic of extrusion based 3D printing process.

Pinch rollers act as the mechanism for driving the filament from the spool, through the heated liquefier, into the nozzle, and onto the build plate. Above these rollers the filament is in tension, pulling on the spool, and below these rollers the filament is in compression.[21] Care is to be taken to maintain a constant volumetric flow rate as to produce a constant extruded road width and thickness. It should be noted that the extruded plastic lines generated during a 3D print are referred to as roads. A critical value for the volumetric flow rate exists as too high a flow rate will cause buckling of material in the compression region below the feed rollers but above the liquefier.[22] However, this buckling is most common with ceramic filaments and much less of a concern regarding plastic filaments such as ABS.[23]

After the material has liquefied it is pushed through the nozzle of the extrusion head where it is then laid on the surface of the build plate. The diameter of the nozzle determines the shape and size of the extruded filament, thereby determining the resolution and minimum feature size of the part. Feature size is approximately equal to two times the diameter of the nozzle.[9]

It is necessary to maintain the nozzle at a height at which it remains in contact with the road it is depositing to produce a print road with a flat top (figure 5).[24] Simulations conducted by Bellini et al found that if the nozzle is above the print road, then it is possible for road distortions to form as a result of die swelling just below the nozzle tip and convective losses.[25]

Solidification of the deposited material occurs when the molten state cools due to convection to the surrounding air and conduction through the build plate/previously deposited layers. To minimize part distortion due to nonlinear/rapid cooling a chamber can be installed around the printer to control the temperature of the environment inside the volume, thus reducing print defects by minimizing the temperature difference between the hot deposited road and the
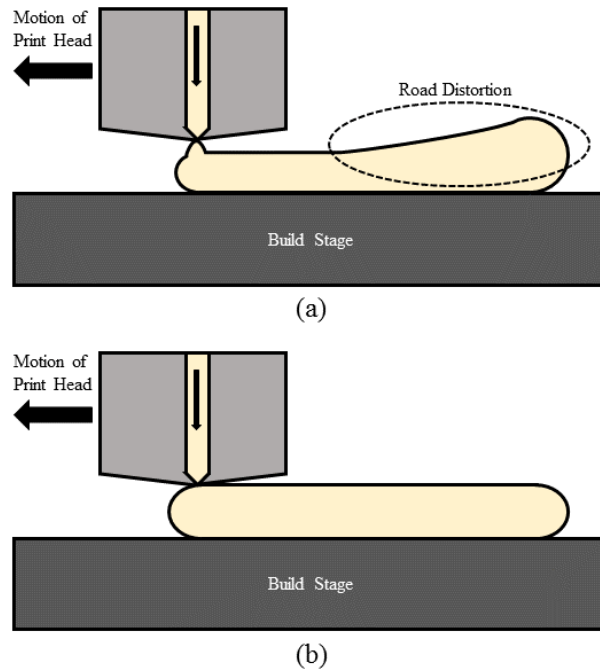
Figure 5. Interaction of extrusion print head with the deposited road. (a) The road shape is distorted when the print head is too far above the deposited road. (b) When the print head is in contact with the deposited road it ensures a flat top road surface.[24]

chamber air.[9] Proper construction of the base layers is critical as any warpage or distortion in these layers will cause an additive effect through the part and is why many FFF printers have a heated print bed/build plate in order to prevent conductive heat loss and distortion. The heated build plate keeps the base layers of the part warm and like a heated build volume allows for more even cooling of the part, thereby reducing and/or preventing part warpage/curling at the base.

Maintenance of extrusion temperature, filament feed rate, and build plate temperature can be set with knowledge of the filament material in the part slicing software, Slic3r. Perhaps most critically, Slic3r is responsible for the slicing of the CAD model to be printed. Slicing is the cutting of the 3D model into horizontal layers and the generation of tool paths to fill them. During this process the software also calculates the material necessary to be extruded for each layer. Material

flow rate for extrusion must be considered in the slicing software as sharp angles in the tool path will require the print head to decelerate and accelerate. If the material flow rate remains constant through acceleration and deceleration events then excess or limited material will be deposited along the tool path respectively.[9]

Temperature control of extruded material and build environment is critical for bonding between layers.[9,24] When material is extruded on top of the road below there must be enough residual heat in the molten bead to activate the adjacent roads as well as the road below in order for bonding to occur. If there is insufficient heat, contacting regions may still adhere, but there is not enough energy to establish bonding between polymers, thereby creating a boundary between the new and previously deposited material. This boundary is a fracture surface where the part can easily be broken/separated.

When designing a part to be printed, overhangs or other free-standing features may be added. In order to successfully print such features, support material is needed to keep them in place. Two general forms exist for support structures, primary or secondary material supports. Primary material supports are supports constructed from the same material the part is fabricated from. Secondary supports are made from a material that is not the material used for fabricating the part. An advantage of secondary support is the ability to place the final print in a solvent bath that dissolves the secondary support material and not the primary material, thus leaving behind the finished part. However, using a material other than the primary material requires use of a second extruder or careful switching of materials via the same extruder. Primary support material is beneficial in that no additional extrusion head or switching between materials is needed. Removal of primary material can become more difficult in post processing as it cannot be easily dissolved away like a secondary material. Temperature controls at support material-part interfaces can be

varied to create a fracture surfaces at these regions thereby making the removal of primary support material easier.

In the chapters that follow the initial heat transfer calculations that established the geometric requirements, design decisions, fabrication and testing of the PHX as it plays a critical role in Rebound's Sunchill refrigeration system will be discussed.

2   Design Calculations

Before a prototype can be built a design is necessary. This design will be rooted in the following calculations of volume, surface area, and geometry and will elucidate the information necessary to construct a prototype in a CAD software package prior to printing.

The constraints of the design of the PHX must first be addressed before discussing the heat transfer calculations of the part. These constraints will contribute to the necessary inputs and assumptions of the following calculations.

The first constraint to be considered is the required internal volume of the part. The necessary volume of the heat exchanger is a product of the cooling demands of the farmer and will ultimately dictate the size/geometry of the PHX.

The second constraint to be considered is the external surface area. The cooling and precipitation of the brine requires the removal of heat. The surface area of the part dictates how much heat can be removed. As was mentioned previously, the heat exchange from the hot brine to the ambient air in the precipitation mode is accomplished via natural convection and the required surface area will be determined using the appropriate correlations. The cooling operation of the PHX demands a double wall system in which water will run in a counter flow configuration (counter flow mode). This leads not only to a geometric requirement of the PHX (double walled) but an additional surface area consideration between the water and brine chambers. The determined counter-flow mode surface area, in conjunction with the volume requirement, will establish a surface area to volume ratio which will act as a geometric constraint that will subsequently dictate the size and geometry of the part.

The final constraint to be considered is the part needs to be 3D printable. Thereby, the design must be printable and capable of fitting in the required build volume. Considerations towards wall thickness, XY and XZ angles, and print speed must also be accounted for as these

will dictate the printability and production time of the part. Given the amount of heat to be removed, it is to be expected that the required surface area in addition to the volume constraint, will not be achieved in the build volume of the selected 3D printer. Thus, in order to meet these requirements, the PHX must be broken down into a repeatable and printable structure. How this is to be achieved will be discussed in the later 3D printing method section.

To summarize, the constraints of the design of the PHX are the required internal volume, the external surface area, a double wall system, and 3D printable interlocking components.

2.1 Required Volume

As previously stated, the required cooling for the farmer will influence the design of the PHX. The two kilowatt demand over four hours yields the energy required, E_{req}, of the system upon dissolution of the salt. The enthalpy of solvation of sodium carbonate decahydrate, ΔH_{solv}, is 241 kJ/kg.[26] For the solid precipitate, sodium carbonate decahydrate, the mass of sodium carbonate and water contained in this species can be found in equations (2) – (4).

$$m_{salt} = \frac{E_{req}}{\Delta H_{solv}} \tag{2}$$

$$m_{Na2CO3} = 0.37 m_{salt} \tag{3}$$

$$m_{H2O} = 0.63 m_{salt} \tag{4}$$

In order to determine the required mass of solution in the PHX as well as the total solution mass in the system, a series of equations must be developed (equations (5) –(9)). From Figure 6 and Figure 7 it can be found that the average nighttime low temperature in Inhambane Mozambique and saturated concentration of sodium carbonate at said temperature are 18°C and 16% m/m (C_{low}) respectively. The spectator salt and water mass, $m_{specNa2CO3}$ and $m_{specH2O}$, is what remains when the 16% m/m evening concentration is reached after 119.5 kg of

Na$_2$CO$_3\cdot$10H$_2$O has precipitated (equation (6)). The inlet of the PHX during the concentration mode is 3-5°C above ambient and the average daily high temperature is 27°C. The corresponding saturation concentration of an aqueous sodium carbonate solution from Figure 7 is 30% m/m (C_{high}). Equation (5) relates the mass of salt and the spectator masses to this high concentration. In order to sufficiently solvate the precipitated, Na$_2$CO$_3\cdot$10H$_2$O to temperatures below the required 10°C as demanded by the farmer the initial concentration at the beginning of the concentration mode is 10% m/m ($C_{dissolve}$).
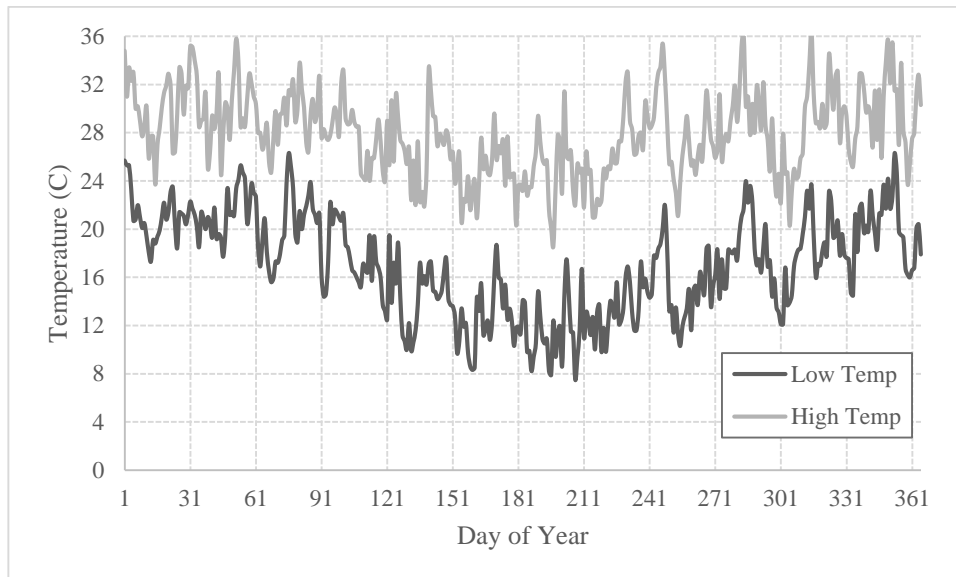
Figure 6. Average daily high and low temperatures in Inhambane Mozambique over one year.
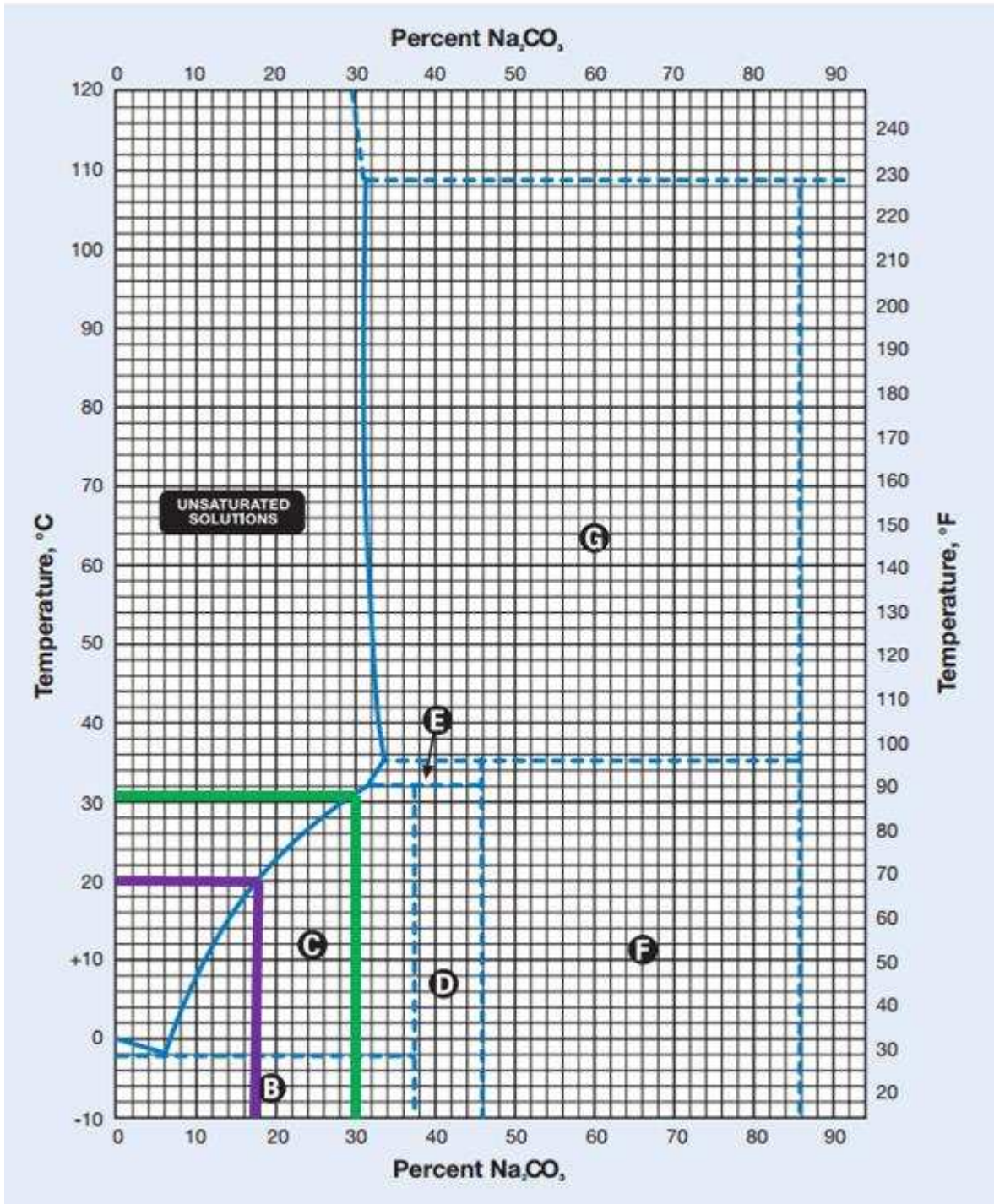
Figure 7. Phase diagram for aqueous sodium carbonate solutions where region (C) produces the solid phase of $Na_2CO_3 \cdot 10H_2O$ when precipitated.[26] The daytime and nighttime saturation concentrations are depicted by the green and purple lines respectively.

$$C_{high} = \frac{m_{Na2CO3} + m_{specNa2CO3}}{m_{Na2CO3} + m_{specNa2CO3} + m_{H2O} + m_{specH2O}} \tag{5}$$

$$C_{low} = \frac{m_{specNa2CO3}}{m_{specNa2CO3} + m_{specH2O}} \tag{6}$$

$$m_{PHX} = m_{Na2CO3} + m_{specNa2CO3} + m_{H2O} + m_{specH2O} \tag{7}$$

$$C_{dissolve} = \frac{m_{Na2CO3} + m_{specNa2CO3}}{m_{Na2CO3} + m_{specNa2CO3} + m_{H2O} + m_{specH2O} + m_{solvH2O}} \tag{8}$$

$$m_{Total} = m_{Na2CO3} + m_{specNa2CO3} + m_{H2O} + m_{specH2O} + m_{solvH2O} \tag{9}$$

$$V_{PHX} = \frac{m_{PHX}}{\rho_{Na2CO3 \cdot 10H2O}} \tag{10}$$

m_{Total} is the total mass of the system. For design purposes of the PHX, the mass necessary to determine the volume of the PHX is m_{PHX}. This is the mass of solution/precipitate that will occupy the brine chamber of the PHX. Solving for m_{PHX} and determining the density of the solution at C_{high} from Figure 8, the required volume of the PHX, equation (10) can be determined. The results of solving equations (2)-(10) are listed in Table 1.
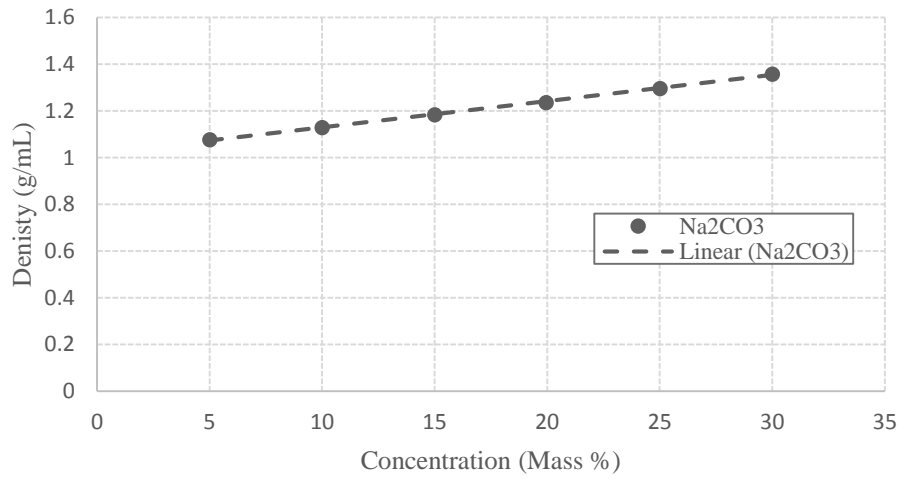
Figure 8. Density vs. concentration of aqueous Na_2CO_3 solutions. Linear fit of the above data yields: $\rho_{Na2CO3} = 0.0112C_{Na2CO3} + 1.0168$.

Table 1. Mass of salt and volume required of PHX	
E_{req}	28.8 MJ
m_{salt}	119.5 kg
m_{Na2CO3}	44.21 kg
m_{H2O}	75.29 kg
$m_{specNa2CO3}$	9.611 kg
$m_{specH2O}$	50.46 kg
m_{PHX}	179.6 kg
$m_{solvH2O}$	359.1 kg
m_{Total}	538.7 kg
V_{PHX}	0.133 m^3

2.2 Surface Area Determination
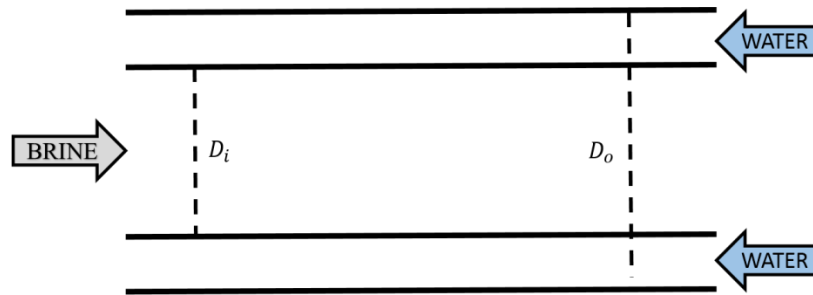
Figure 9. Schematic of PHX with double wall system where water flows in a counter flow configuration.

Utilizing the above information, the necessary inputs for the problem can be found in Table 2. Figure 9 illustrates a simple schematic of the described concepts of the PHX. The volume of the brine solution is contained in the central chamber. Cooling water flowing in a counter flow configuration is contained in the outer chamber. Symmetry in the PHX can reduce the complexity of the problem by simplifying the problem to one half of the PHX schematic (figure 9), divided along the length of the brine chamber. This will simplify the resistance network for the system to that in figure 10. Here, L_{brine} and $L_{WaterGap}$ are taken to be the length, L, of a horizontal rectangular cavity, see figure 9. Reducing the problem in this manner establishes the hot side of the network at the bottom of the schematic where the temperature at this point is the average bulk temperature of the brine, $T_{infBrine}$. Due to this, it is assumed that the brine and water chambers are horizontal cavities heated from below and heat is transferred via natural convection in these cavities. Varying L_{brine} and $L_{WaterGap}$ over the printable range given the XY build plate dimensions of 298mm x 275mm, it can be found in figures 11-13 that the required surface area increases over small values of L but remains constant for larger values.
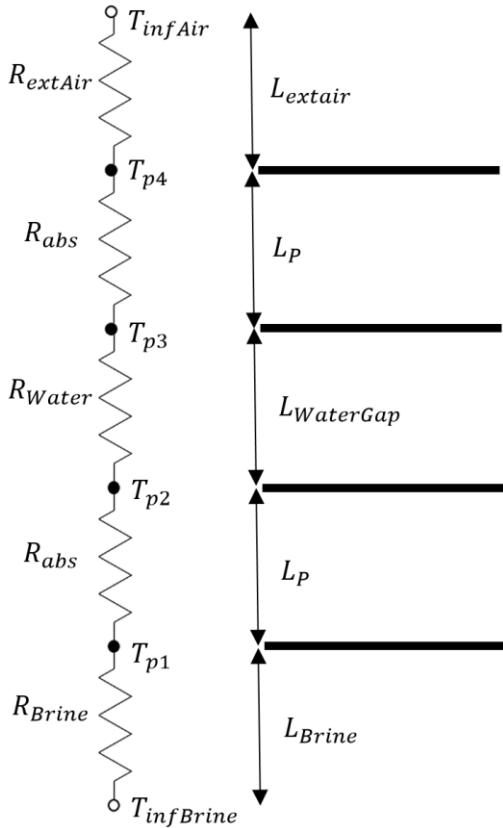
Figure 10. Resistance network of PHX. Note: Dimensions not to scale.

Table 2. Heat transfer calculation inputs

Physical Constants

g	9.81 m/s^2

Environmental Inputs

$T_{infBrine}$	30°C
T_{infAir}	18°C
P	101.3 kPa

Solution/Equipment/Experiment Inputs

m_{PHX}	179.6 kg
m_{salt}	119.5 kg
ΔH_{sol}	241 kJ/kg
Cp_{brine}	3.6 kJ/kg-K
C_{brine}	30 % m/m
K_{abs}	0.17 W/m-K
t_{precip}	12 hrs

Geometric Inputs

L_{brine}	1.5 cm
L_P	1.5 mm
$L_{WaterGap}$	1 cm
L_{extAir}	1 m

It is assumed the external air acts via natural convection over a hot, horizontal surface, hence, L_{extAir} is the characteristic length of free convection above a hot plate and is defined as the ratio between the surface area to the perimeter and thus has units of meters. It can be determined from figure 14 that for a surface area to perimeter ratio less than 0.3 m, the surface area decreases. For a surface area to perimeter ratio above 0.3 m, the surface area remains constant. The input value of L_{extAir} in the following calculations is then taken to be one meter in order to overestimate the surface area.

The thickness of the plastic walls, L_P, effects the surface area of the PHX linearly due to conduction. As wall thickness increases the required surface area of the PHX increases. It will be

discussed in sections following that the ideal printed part must have the least number of print beads (number of print lines per wall) while maintaining rigidity, have few print errors, and print in a time efficient manner. From print testing on the LulzBot TAZ 4, it was found that the optimum (and largest available) print head is 0.75mm and the least number of print roads as was 2. Thus, resulting in a value of 1.5 mm for L_P.
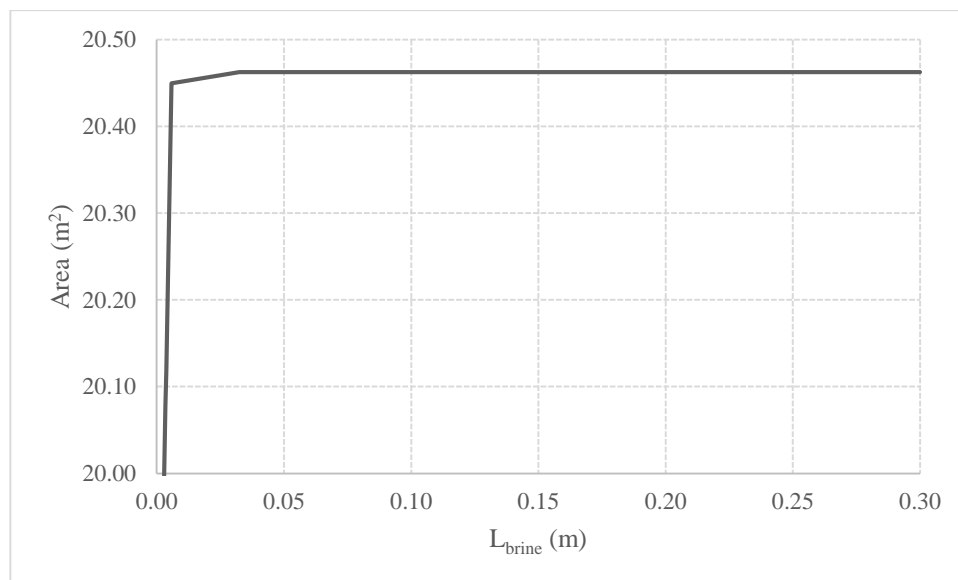
Figure 11. Surface area of PHX as function of brine chamber "height".
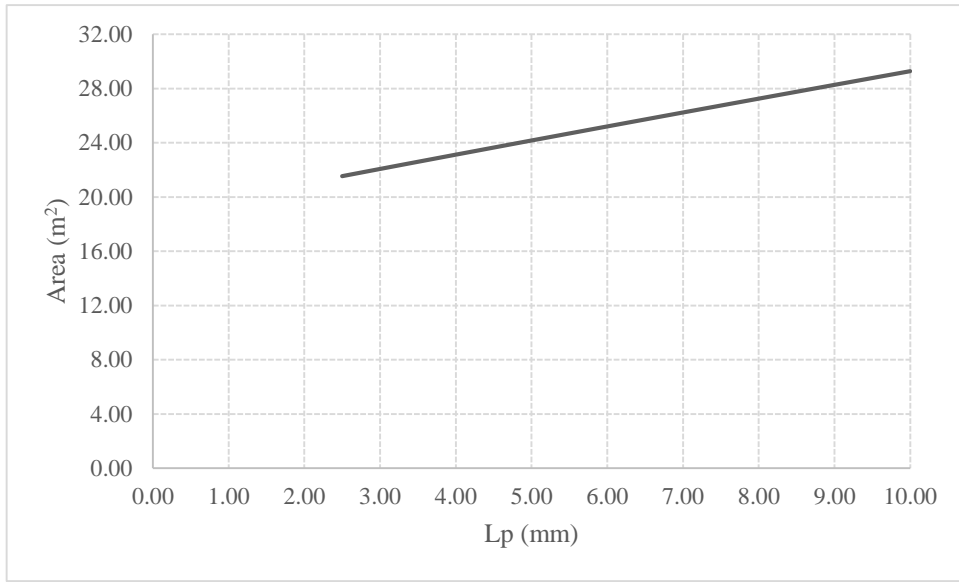
Figure 12. Surface area of PHX as function of abs plastic wall thickness.
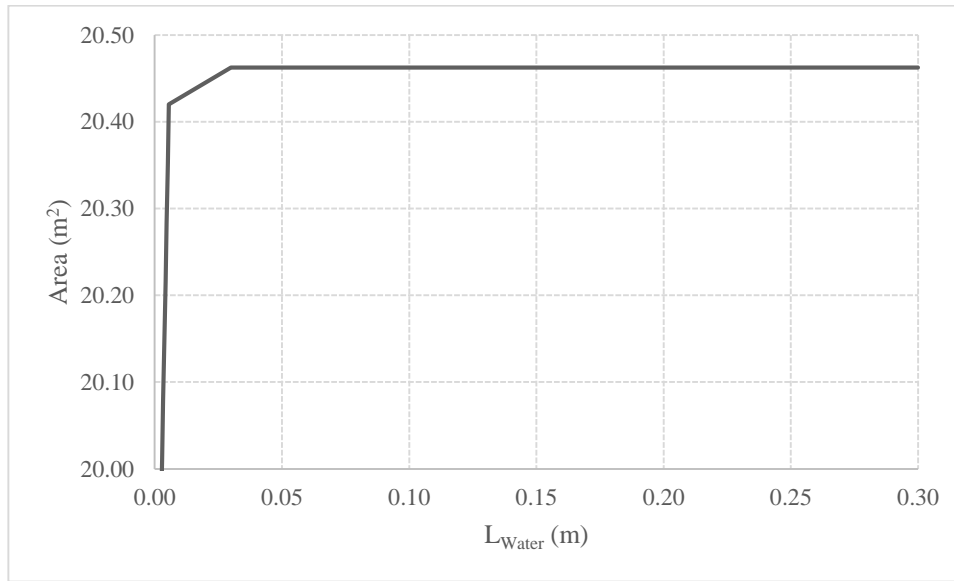
Figure 13. Surface area of PHX as function of water chamber "height".
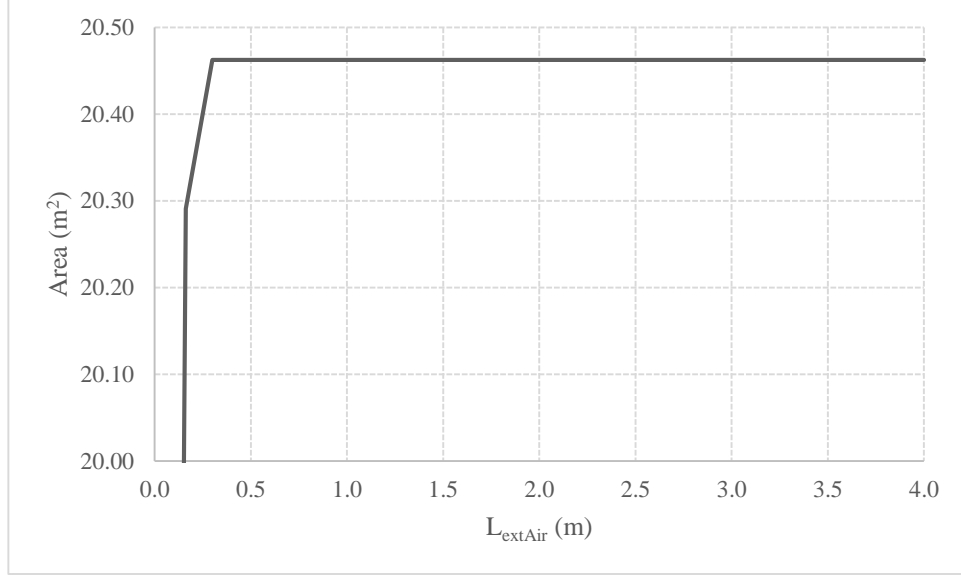
Figure 14. Surface area of PHX as function of external air characteristic length. Where the ratio of $L_{extAir} = \frac{Surface\ Area}{Perimeter}$.

During the twelve hour period in the evening of which the precipitation process is to occur the heat required to dump to the ambient air is the sum of the 30°C solution that initially fills the brine chamber, q_{sol}, as well as the heat of precipitation, q_{precip}. The solvation of $Na_2CO_3 \cdot 10H_2O$ is endothermic and thus the precipitation of said salt must be exothermic. The required heat transfer can be found by solving equations (11)-(14).

$$Q_{sol} = m_{PHX}\, Cp_{brine}(T_{infbrine} - T_{infAir}) \tag{11}$$

$$Q_{precip} = m_{salt}\Delta H_{sol} \tag{12}$$

$$Q_{total} = Q_{sol} + Q_{precip} \tag{13}$$

$$\dot{Q} = \frac{Q_{total}}{t_{precip}} \tag{14}$$

As mentioned previously, the brine chamber is modeled as a horizontal cavity heated from below. This gives τ=0° in figure 15. Assuming
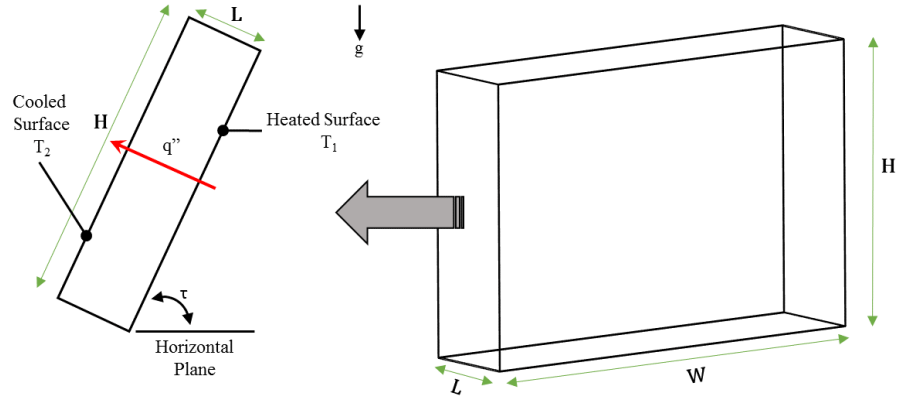
Figure 15. Natural convection in rectangular cavity.[8]

H/L and w/L are greater than one and finding the Raleigh number for this chamber is greater than the critical value of 1708 (equation (15)), the approximation of the average convection coefficient of the brine chamber can then be found using the Globe and Dropkin correlation in equation (16).

$$Ra_{brine} = \frac{g\beta}{v\alpha}(Tinf - Tp1)L_{brine}{}^3 \tag{15}$$

$$\overline{Nu}_{brine} = \frac{\bar{h}_{brine}L_{brine}}{k_{brine}} = 0.069 Ra_{brine}{}^{1/3} Pr_{brine}{}^{0.074} \tag{16}$$

$$R_{brine} = \frac{1}{\bar{h}_{brine}A} \tag{17}$$

$$\dot{Q} = \frac{(T_{infBrine} - T_{p1})}{R_{brine}} \tag{18}$$

Necessary property values are most similar to potassium carbonate, K_2CO_3, in the EES brine library. The interior abs plastic wall is modeled as conduction, equation (19).

$$R_{abs} = \frac{L_p}{k_{abs}A} \tag{19}$$

$$\dot{Q} = \frac{(T_{p1} - T_{p2})}{R_{abs}} \tag{20}$$

The outer chamber designated as the cooling water flow path (see figure 9) during the solvation step is in this "precipitation mode" filled with ambient water and left stagnant over twelve hour duration. Due to the quiescent nature of the water, this chamber can also be modeled as natural convection in a horizontal cavity heated from below using equations (21)-(24).

$$Ra_{Water} = \frac{g\beta}{\nu\alpha}(Tp2 - Tp3)L_{Water}{}^3 \tag{21}$$

$$\overline{Nu}_{Water} = \frac{\bar{h}_{Water}L_{Water}}{k_{Water}} = 0.069Ra_{Water}{}^{1/3}Pr_{Water}{}^{0.074} \tag{22}$$

$$R_{Water} = \frac{1}{\bar{h}_{Water}A} \tag{23}$$

$$\dot{Q} = \frac{(T_{p2} - T_{p3})}{R_{Water}} \tag{24}$$

The exterior plastic wall is modeled the same as previous since it is assumed the thickness for the interior and exterior walls is identical.

$$\dot{Q} = \frac{(T_{p3} - T_{p4})}{R_{abs}} \tag{25}$$

It will be assumed the external ambient air is quiescent. This will yield an overestimation in the required surface area as the heat transfer coefficient for natural convection will be lower

than a forced convection heat transfer coefficient, thereby increasing the thermal resistance and subsequently the surface area. The ambient air will therefore be modeled as the upper surface of a horizontal "hot" plate. Taking equation (26) and finding a Raleigh number of 10^9 the proposed correlation to model the external air is given in equation (27) by McAdams.

$$Ra_{Air} = \frac{g\beta}{\nu\alpha}(Tp4 - TinfAir)L_{Air}^3 \tag{26}$$

$$\overline{Nu}_{Air} = \frac{\bar{h}_{Air}L_{Air}}{k_{Air}} = 0.15Ra_{Air}^{1/3} \tag{27}$$

$$R_{Air} = \frac{1}{\bar{h}_{Air}A} \tag{28}$$

$$\dot{Q} = \frac{(T_{p4} - T_{infAir})}{R_{Air}} \tag{29}$$

The results for solving this nodal network are listed in Table 3. The required surface are of the PHX given the required energy to remove from the brine solution overnight is 20.46 square meters. Taking the volume to be 0.133 m³, the surface area to volume ratio for the PHX is 154. This provides the design parameter for the size of the part when building in a CAD software package. In the sections following, the shape and other geometries of the PHX will be investigated.

Table 3. *Heat transfer calculation results*

T_{p1}	29.58°C
T_{p2}	28.18°C
T_{p3}	28.78°C
T_{p4}	28.37°C
q_{sol}	7.76×10^6 J
q_{precip}	2.88×10^7 J
q_{total}	3.66×10^7 J
$\dot{Q}$	846 W
Ra_{brine}	2.94×10^4
$\bar{h}_{brine}$	98.73 W/m²K
R_{brine}	4.95×10^{-4} K/W
R_{abs}	4.31×10^{-4} K/W
Ra_{Water}	1.03×10^4
$\bar{h}_{Water}$	102.7 W/m²K
R_{Water}	4.76×10^{-4} K/W
Ra_{Air}	9.87×10^8
$\bar{h}_{Air}$	3.958 W/m²K
R_{Air}	0.0124 K/W
A	20.46 m²

Construction of the PHX is required to be done by means of 3D printing and thus plastic will be the material of choice as the method for printing will be fused filament fabrication (FFF). ABS is chosen for its higher glass transition temperature when compared to the common alternative printing filament, PLA. It may at first appear that plastic would be a poor choice for this heat exchanger due to its low thermal conductivity, as most commercial heat exchangers are made of metal, namely copper which has a comparatively high thermal conductivity of 401 W/m-K.[27] However, for this system, the thermal resistance pinch point is not the conduction through the walls of the part but rather the natural convection to the external ambient air. The significant difference between the external air resistance and all other resistances can be seen in figure 16 over increasing wall thickness. As stated prior, the determined surface area of the PHX is 20.46 m^2. If
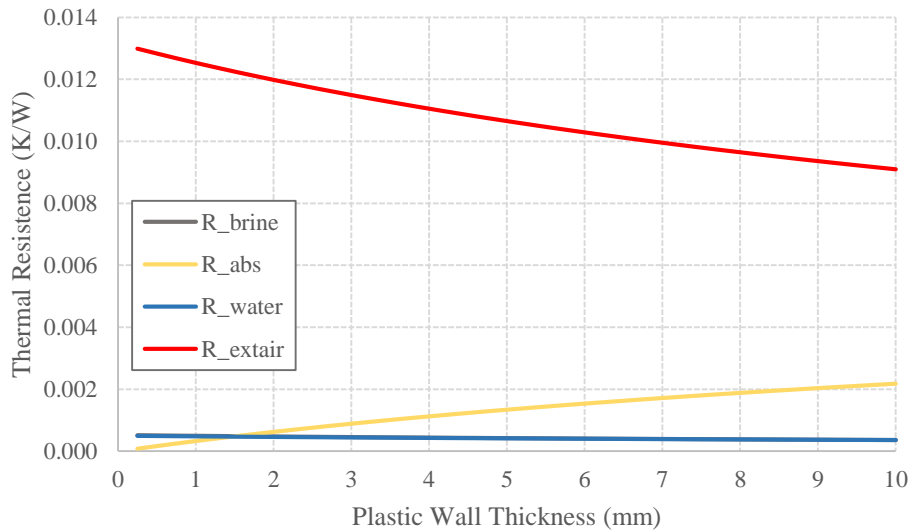
Figure 16. Thermal resistance of PHX components as function of plastic wall thickness.

one were to substitute the thermal conductivity of copper for the thermal conductivity of ABS plastic the surface area would only be reduced to 18.83 m^2. This results in a minor 8% decrease in surface area.

The experimentally determined wall thickness of 1.5 mm yields a resistance for the ABS walls that is less than all other resistances in the network (see Table 3 and Figure 16). It can be found in figure 17 that in order for the plastic wall to become the pinch point of the system, that is to have a resistance higher than the external air, the walls would need to be 53 mm thick. Therefore, to reduce the surface area required to remove the heat of the hot brine, one would need to design the PHX in such a way as to reduce the thermal resistance of the external air.
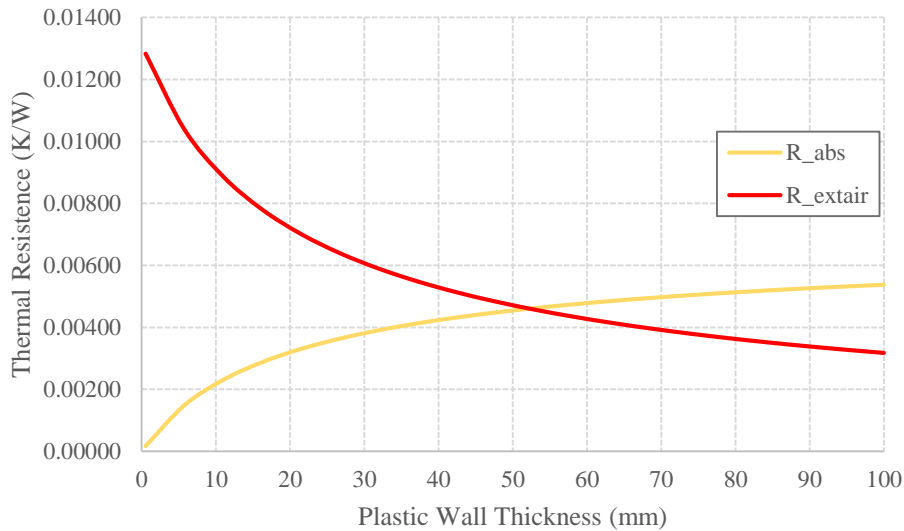
Figure 17. Comparison of plastic wall and external air resistances over increasing wall thickness.

2.3 Shape Determination

The search space for determining a shape for the PHX is endless and therefore only basic geometries will be investigated. The leading assumption in this investigation is the PHX is a single pipe of presumably long length with the face of the specified shape. From the required surface to volume ratio the required shape size and pipe length can be determined.

Using the surface area to volume ratio as an input the required diameter and length of a cylindrical pipe can be found by solving equations (30)-(33). Equations (32) and (33) can be modified for triangular, square, and hexagonal faces by using the face area and perimeter equations for these shapes found in equations 33-38.

$$A_{cylFace} = \pi(\frac{D}{2})^2 \tag{30}$$

$$Perimeter_{cyl} = \pi D \tag{31}$$

$$SA = Perimeter * L + 2A_{cylFace} \tag{32}$$

$$L = \frac{V}{A_{cylFace}} \tag{33}$$

Equilateral Triangle

$$A_{triFace} = \frac{\sqrt{3}}{4} b^2 \tag{34}$$

$$Perimeter_{tri} = 3b \tag{35}$$

Square

$$A_{sqFace} = a^2 \tag{36}$$

$$Perimeter_{sqFace} = 4a \tag{37}$$

Hexagon

$$A_{hexFace} = 1.5\sqrt{3}\, s^2 \tag{38}$$

$$Perimeter_{hexFace} = 6s \qquad\qquad (39)$$

The results for solving the above for each shape's characteristic dimension and pipe length are given in Table 4. The characteristic dimensions given here for a cylinder, equilateral triangle, square, and hexagon are diameter (D), base (b), side (a), and side (s), respectively. It would appear from this initial calculation that an equilateral triangular shape would yield the shortest pipe length part, thereby potentially reducing the number of prints and subsequently a shorter overall print time. However, upon printing triangular test coupons of 4.5 cm at higher print speeds than default settings, it was found that the sharp 60° angle of the corners resulted in significant print errors and a non-waterproof part. The print defects at the corners were due to the increased deceleration and acceleration events associated with acute angles. In order to be a viable option, the shape of the part must allow the printer to use a fast print speed while minimizing print errors/defects.

After investigation into the literature regarding print angles and their relative print speeds it was found that hexagons would be most promising in providing the necessary results.[9,24] Increasing print speed of a tool path that contains acute angles requires substantially more deceleration and acceleration of the extrusion print head. This can lead to under and/or over extrusion of material at these sites due to the inability of material feed system to compensate for the acceleration and deceleration events. The observed print errors at the corners of the triangle coupons was an example of this phenomena. After multiple small hexagon coupon tests, it was found that a hexagon shape could provide a much faster print time than triangles while maintaining a waterproof character. The obtuse, 120° angle of the hexagon tool path did not require the deceleration or acceleration to navigate the corners as the triangular tool path. Therefore, due to the ability of increased print speed, a hexagon shape with side length of 1.5 cm and diameter of 3

cm was chosen. The choice of hexagons due to their printing characteristics is discussed in further

detail in chapter 3.

Table 4. Characteristic dimensions and required lengths
of various shaped pipes to achieve required surface area
to volume ratio.

Shape	Characteristic Dimension	Length
Cylinder	D = 2.6 cm	250 m
Triangle	b = 4.5 cm	152 m
Square	a = 2.6 cm	197 m
Hexagon	s = 1.5 cm	227 m

2.4 Pipe Spacing

It is known for vertical open channels in a quiescent fluid with large height (L) to spacing (S) ratio

(L/S), the boundary layers of the opposing surfaces converge, thereby establishing a fully

developed condition. As spacing increases, the boundary layer convergence disappears and the

boundary layer formation on the opposing surfaces is independent, like that of an isolated plate.[8]

In other words, keeping L constant and providing a large spacing, the natural convection heat

transfer coefficient will be identical to that of an isolated vertical plate. It can then be predicted

that as the spacing between these surfaces decreases so will the heat transfer coefficient.[28]

In this case the previously determined 3 cm diameter hexagon pipe will be assumed to be a vertical

plate with surface temperature of Tp4. To determine the optimal pipe spacing, the correlation,

equation (44), developed by Elenbaus for vertical channels in a quiescent fluid, will be used where

L=3 cm. Figure 18 illustrates that at high values for spacing, S, the heat transfer coefficient is

constant and of that of an isolated vertical plate with the same surface area. As S is decreased, the

heat transfer coefficient also decreases. The optimum spacing for a vertical channel of height 3 cm and the specified temperature difference is determined to be 1.3 cm.
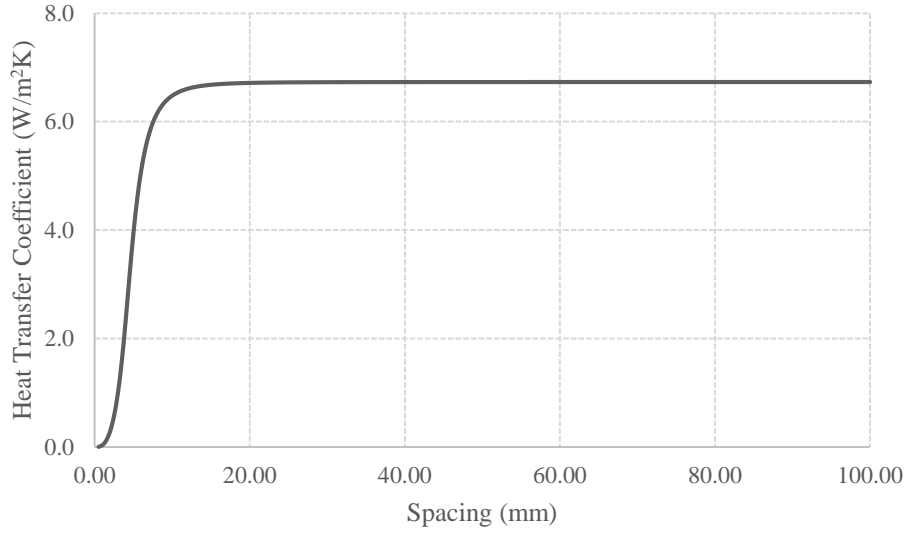
Figure 18. Heat transfer coefficient as function of spacing of vertical channel of height 3 cm, surface temperature of $Tp4$ and infinite temperature of T_{infAir}.

$$Ra_S = \frac{g\beta(T_s - T_\infty)S^3 Pr}{\nu\alpha} \tag{42}$$

$$\overline{Nu_S} = \frac{\overline{h_s}S}{k} = \frac{Ra_S}{24\left(\frac{L}{S}\right)}\left(1 - exp\left[\frac{-35\left(\frac{L}{S}\right)}{Ra_S}\right]\right)^{3/4} \tag{43}$$

In summary, to transfer the required heat over the allotted twelve hour night time period the required PHX must have a surface area of 20.46 m², a volume of 0.133 m³, resulting in an

optimum pipe shape of 3 cm hexagon tubes oriented with faces into air flow, and a spacing between pipes of 1.3 cm.

2.5 Counter Flow Surface Area Requirement

To provide the required cooling to water that will chill crops the following morning, the PHX must operate as a counter flow heat exchanger. In the early morning hours as the precipitate is solvated with the previously removed water from the concentration step, the solution becomes cool as the dissolution of $Na_2CO_3 \cdot H_2O$ is endothermic. Flowing counter to this process in the "water chamber" (surrounding the brine chamber) is the water that will chill the morning's harvested crops. The following is the determination of the required surface area of the plastic wall that separates the brine and water chambers. It is assumed for simplicity in modeling that the brine chamber is a circular pipe with diameter D=3 cm, and the water chamber is an annulus that surrounds the inner brine chamber.

From the demands of the farmer it is known that 2 kW of heat must be removed from the water stream and the outlet of this chilled water must be 10°C ($T_{out,w}$). Given the inlet ($T_{in,w}$) is ambient at 20°C, the mass flow rate of the water path can be found using

$$\dot{Q} = \dot{m}_{water} Cp_{water} (T_{in,w} - T_{out,w}). \tag{45}$$

Assuming all the heat removed from the water is transferred to the brine and that the mass flow rate of the brine is the same as the water mass flow rate, equation (46) can be written as

$$\dot{Q} = \dot{m}_{brine} Cp_{brine} (T_{in,b} - T_{out,b}). \tag{46}$$

Using the determined mass flow rate, the Reynolds number for the brine flow through the interior pipe can be determined in equation (47). It is found the flow through the 3 cm diameter

interior brine chamber is laminar, Re < 2300. For laminar flow through a circular tube the average friction factor proposed by Shah and London is given by equation (48). This friction factor can be used to calculate the pressure drop (equation (50)). Entrance and exit effects are neglected here and a long straight pipe with no inertial losses is assumed.

$$Re = \frac{4\dot{m}}{\pi D \mu} \tag{47}$$

$$\bar{f} = \frac{4}{Re}\left[\frac{3.44}{\sqrt{L^+}} + \frac{\frac{1.25}{4L^+} + \frac{64}{4} - \frac{3.44}{\sqrt{L^+}}}{1 + \frac{0.00021}{(L^+)^2}}\right] \tag{48}$$

$$L^+ = \frac{L}{D_h Re} \tag{49}$$

$$\Delta P = \frac{\bar{f} L \dot{V} \rho}{2D} \tag{50}$$

$$\dot{V} = \frac{\dot{m}}{A_c \rho} \tag{51}$$

$$A_c = \pi \left(\frac{D}{2}\right)^2 \tag{52}$$

For laminar flow through a circular pipe the Nusselt number does not depend on surface roughness but rather the dimensions of the pipe.[29] Assuming constant heat flux from the brine to water chambers, the correlation given by Hornbeck is:

$$\overline{Nu}_H = \frac{\bar{h}_{Inner} D}{k} = 4.36 + \frac{\left[0.1156 + \frac{0.08569}{Pr^{0.4}}\right] Gz}{[1 + 0.1158 Gz^{0.6}]} \tag{53}$$

$$Gz = \frac{DRePr}{L} \tag{54}$$

The water chamber that surrounds the internal brine chamber of the PHX will be assumed to be a circular annulus for purposes of determining an estimate of the required surface area. The Reynolds number for internal flow through an annulus is given by equation (55). In accordance with the previous calculations, the pressure drop through the water chamber is estimated by equation (58) and the average friction factor is determined by equation (57) using the local friction factor for laminar hydrodynamically fully developed flow (equation (56)).

$$Re_{D_h} = \frac{\dot{m}D_h}{A_c \mu} \tag{55}$$

$$f_{fd,h} = \frac{64}{Re_{D_h}} \sqrt{\frac{\left(1 - \left(\frac{r_i}{r_o}\right)^2\right)}{1 + \left(\frac{r_i}{r_o}\right)^2 - \left(\frac{1 - \left(\frac{r_i}{r_o}\right)^2}{\ln\left(\left(\frac{r_i}{r_o}\right)^{-1}\right)}\right)}} \tag{56}$$

$$\bar{f} \approx \frac{4}{Re_{D_h}} \left[\frac{3.44}{\sqrt{L^+}} + \frac{\frac{1.25}{4L^+} + \frac{f_{fd,h}Re_{D_h}}{4} - \frac{3.44}{\sqrt{L^+}}}{1 + \frac{0.00021}{(L^+)^2}} \right] \tag{57}$$

$$\Delta P = \frac{\bar{f}L\dot{V}\rho}{2D_h} \tag{58}$$

$$A_c = \pi(r_o^2 - r_i^2) \tag{59}$$

$$D_h = \frac{A_c}{2\pi(r_i + r_o)} \tag{60}$$

The determined Reynolds number is found to be laminar, Re $<$ 2300, over a range of outer diameter values (figure 19). The appropriate average Nusselt number for laminar flow through an annulus is given in equation (65) by Shah and London.[30]

$$\overline{Nu}_{fd,H} = \frac{0.5965}{\binom{r_i}{r_o}} + 6.159 - 3.393\binom{r_i}{r_o} + 2.090\binom{r_i}{r_o}^2 \tag{61}$$

$$DNu_H = 1.55\left(1.754 exp\left(-0.4028 ln(L^*)\right)^{1.050}\right) \tag{62}$$

$$L^* = \frac{L^+}{Pr} \tag{63}$$

$$DNurat = 0.6847 + 0.3153 exp\left(-1.2654\left(\ln(Pr) - \ln(0.72)\right)\right) \tag{64}$$

$$\overline{Nu}_H = \frac{\bar{h}_{Annulus} D_h}{k} = \overline{Nu}_{fd,H} + DNurat\overline{DNu}_H \tag{65}$$
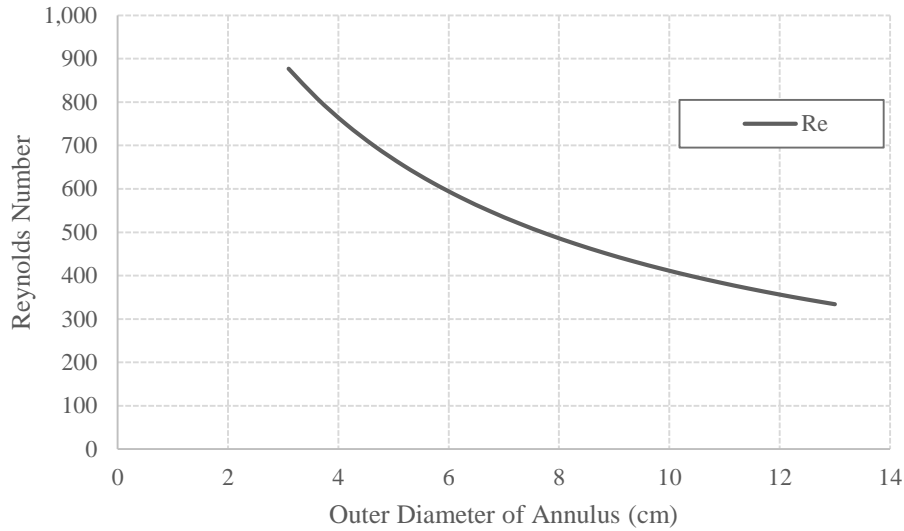
Figure 19. Reynolds number for internal flow through annulus water chamber as function of outer diameter. Inner diameter is fixed at 3 cm.

Taking the previously determined heat transfer coefficients, an over heat transfer coefficient, U, can be calculated.

$$U = \frac{1}{\dfrac{1}{\bar{h}_{Inner}} + \dfrac{1}{\bar{h}_{Annulus}}} \tag{66}$$

Equation (67) and (69) can now be used to determine the required length of the length and area of the interior wall of the PHX to deliver 2 kW of cooling to the water stream to subsequently chill harvest crops. Inlet and outlet temperatures to determine the log mean temperature difference (equation (68)) are denoted as subscripts in and out respectively and water and brine chambers as subscripts w and b respectively. Figure 16 demonstrates the proportionality between outer diameter size and required surface area.

$$q = U\Delta T_{lm}A \tag{67}$$

38

$$\Delta T_{lm} = \frac{\left(\left(T_{in,w} - T_{in,b}\right) - \left(T_{out,w} - T_{out,b}\right)\right)}{ln\left(\frac{\left(T_{in,w} - T_{in,b}\right)}{\left(T_{out,w} - T_{out,b}\right)}\right)}$$

(68)

$$A = \pi D_i L_{pipe}$$

(69)
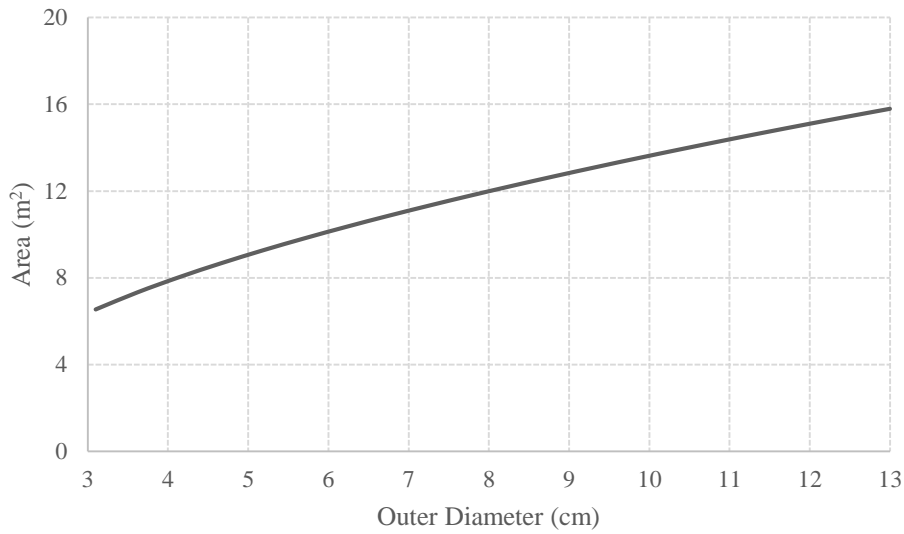
Figure 20. Required surface area of PHX in counter flow "mode" to deliver 2kW of cooling to water stream as a function of outer diameter. i.e. increasing the size of the water chamber.

The necessary surface area of the PHX for the effective precipitation of $Na_2CO_3 \cdot H_2O$ as previously determined was 20.46 m^2. In figure 20, the required surface area in counter flow mode is less than 20.46 m^2 over the provided range of outer diameters. It can be inferred then, that any outer diameter greater than 3 cm will provide effective heat transfer between water and brine streams, given that the pressure drop is not significantly high (smaller outer diameter). Figure 21 illustrate the dependence of pressure drop across the water chamber on chamber size. In order to minimize pressure drop, print material/time, and to accommodate ¼" threaded hose barbs that

39

support the piping of the rest of the system, an outer diameter of 5 cm is chosen. This results in a

1 cm gap requirement between the inner brine chamber wall and the outer wall of the PHX.
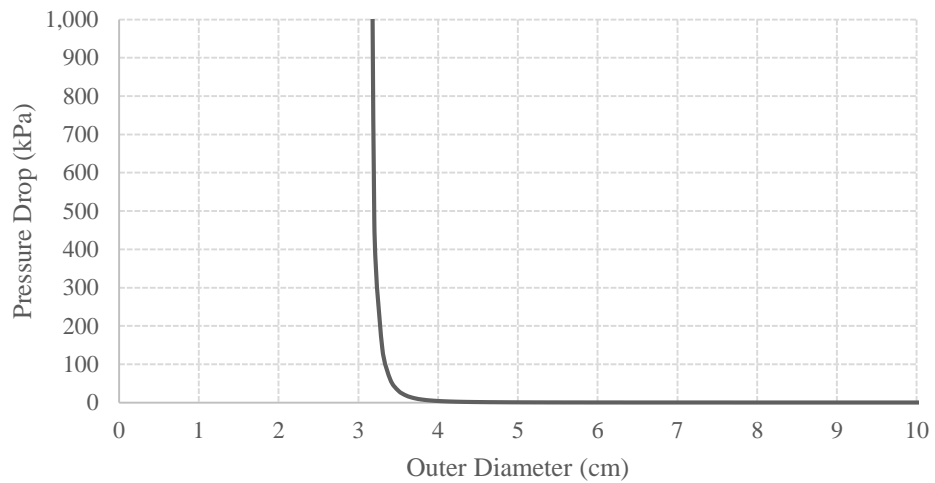
Figure 21. Pressure drop across water chamber as function of outer diameter.

It conclusion of the preliminary calculations, in order to achieve the necessary specifications in

precipitation and counter flow modes the geometry of the PHX is as follows:

- Surface Area:Volume $\geq$ 154.

- 3 cm diameter hexagonal pipe inner brine chamber.

- 1 cm gap between inner brine chamber wall and outer wall to create the water chamber (5 cm diameter hexagon surrounding brine chamber).

- 1.3 cm spacing between pipes in an array.

3   Fabrication: 3-D Printing and Thin Film ABS Deposition

3-D printing is an additive manufacturing technique that was introduced in the late 1980's with the advent of a laser curing system known as stereolithography (SLA).[9] SLA uses the focused beam of an UV laser to solidify a liquid resin bath, layer by layer. Due to the small spot size of the focused beam and the cured layer depth, SLA machines produce high resolution parts. However, these printers are relatively slow, expensive due to the liquid polymer resin, and the cured photopolymer deteriorates over time. The more cost effective, robust, and rapid printing method for fast prototyping is fused filament fabrication (FFF).

FFF machines operate by liquefying a solid polymer filament and extruding the material onto a build surface; constructing the part layer by layer in the same fashion as SLA. Although FFF has a lower resolution, its low cost, relatively short print time, and selection of polymer filaments make it an attractive choice for this project.

The most common choices for the polymer filament for FFF are acrylonitrile butadiene (ABS) and polylactic acid (PLA) but a wide range of polymer filaments exists. Much like the photopolymers used in stereolithography, PLA photodegrades overtime and becomes thermally unstable at temperatures approaching its glass transition temperature.[31,32,33] The glass transition temperatures of ABS and PLA are 105°C and 58°C respectively.[34,35,36] The PHX will be utilized in an outdoor application which dictates the PHX needs to be constructed of a robust material that will not degrade in the lifetime of the Sunchill[TM] system. To avoid any thermal warping or photo-degradation, ABS was the filament of choice for this project due to its mechanical reliability, higher glass transition temperature and its ability to dissolve readily in acetone for use as a post processing technique that proved key in developing a waterproof part.

The initial goals for the 3D printing/prototyping portion of this project were to achieve a part that is waterproof off of the printer. That is, the part can be removed directly from the printer,

filled with water and not leak. The part must print in a time efficient manner. Finally, due to the estimated volume required of the heat exchanger, the final PHX must be capable of being assembled via interlocking components as the build volume of the printer is significantly less than that of the required volume of the PHX. The development of test coupons to full size components and the interplay between the aforementioned goals will be discussed in what follows.

3.1 Preliminary Test Coupons

In interest of time efficient printing and heat transfer it was determined that the PHX would need to be thinned walled. In order to achieve this, the CAD for the part would be constructed in such a manner as to alleviate the need for infill while printing the walls of the part. From the initial results of calculations, equilateral triangles with 4.5 cm sides yielded the shortest overall length required of the PHX, meaning the fewest required components and shortest overall print time. Thus, this shape was adapted into a test coupon with 1 mm walls that could then be filled with a small amount of water to test for leaks off the printer. Printing of these coupons were conducted using a MakerBot Z18 printer with a 0.3 mm nozzle resulting in 3 print roads per wall (figure 22). The fine nozzle used for these tests required a high number of print roads and subsequently a long print time of 30 min relative to the small size of the part. One out of five attempts of this coupon were waterproof off the printer. It was found that increasing print speed would induce increased layer-layer bonding issues at the sharp, acute 60 degree corners of the equilateral triangle tool path. It is suspected that the increased print speed caused an insufficient amount of material to be deposited, such that bonding was not fully achieved at these regions; thereby creating fracture points that water could permeate. Separation and print defects at the corners were the source of water leaking from the part, thus a design that allows for faster print speeds while maintaining a waterproof character was needed.

Figure 22. Equilateral triangle test coupon with 1 mm walls.

The inability to produce consistent waterproof coupons from the triangle tests resulted in additional calculations to determine another geometry. It was found that a hexagon with a 1.5 cm side would provide the necessary heat transfer. A small scale coupon of 1:3 was developed for rapid prototyping and testing to determine print settings and part design failures (figure 23). Hexagons were not only appealing from the results of the calculations but also that the obtuse 120 degree corners offered less print errors at the apexes. The tool path for a hexagon allowed for faster print times without the warping/defects present in the triangular path. It is suspected that the shallow angles of the hexagon tool path allow for more level deposition of each layer at higher print speeds as acceleration and deceleration events are minimized in such a tool path. The sharp corners of the triangular tool path require the print head to rapidly decelerate into and accelerate out of the apex. If material flow rate is not adjusted to compensate for such events, it is possible

Figure 23. Hexagon test coupon.

for a buildup or loss of layer height to occur at these sites. Subsequently causing the points of leakage previously observed. All small hexagon coupons were found to be waterproof off of the printer.

It is noted that the MakerBot Z18 could only be used with MakerBot's proprietary software that does not allow for user manipulation of machine controls such as material feed rate, layer thickness, and road overlap. The lack of such user control over the extrusion, temperature, and tool path eventually lead to the selection of a replacement printer. With the desired controls in mind as well as the ability to repair/modify a printer to produce the required print characteristics resulted in the selection of the open source, locally manufactured (Loveland CO) printer, the Lulzbot Taz 4.

3.1.1 Slic3r: G-code Generator for 3-D Printing

The Lulzbot Taz 4 can easily be used with G-code instructions for printing from the slicing software called Slic3r. Slic3r takes the 3-D CAD model the user has constructed and cuts it into many horizontal cross sections or layers of thickness of the printer's resolution, constructs tool paths to fill these layers and the amount of material that needs to be extruded. The software contains many controls and since many were left to default values, the key controls manipulated for successful printing of the PHX will be discussed here. For the full list of controls and

definitions, please refer to the Slic3r manual listed in the references.[37] The key parameters critical for the printing of the PHX were vertical shell perimeters, speed of perimeters, speed of external perimeters, speed of bridging, first layer speed, default extrusion width, first layer extrusion width, perimeter extrusion width, and overlap.

Definitions of key Slic3r parameters:

Vertical shell perimeters: Sets the number of roads a wall in a print will have. Most parts use infill, such as the endcaps printed for the full size PHX prototypes, and perimeters simply trace the outline of the part the designated number of times. This parameter is typically set to a value of 2 in order to insure quality exterior part surface.

Speed of perimeters: Print speed for perimeters. Default value of 60 mm/s.

Speed of external perimeters: Print speed for the external, visible perimeters. The default value is set to 50% relative to the speed of perimeters.

Speed of bridging: Print speed for bridges. Bridges are produced when no support material is added and it is necessary to bridge a gap/create an overhang in the part. Default value set to 50 mm/s.

First layer speed: Print speed of bottom, first printed layer. The default value is set to 30% of the default speed and is typically set to a low speed to insure proper first layer adherence to the build plate. Without such, the part may warp and bow up, separating from the build plate resulting in either a poorly printed part or a part that detaches from the build plate and the remaining extrusion is printed in free space resulting in a large filament ball of "yarn". The default speed in this case being the speed of perimeters. First layer speed is critical to successful printing of the rest of the part.

Default extrusion width: Sets a manual extrusion width of the extruded road. All extrusion width default values are calculated based on nozzle diameter by Slic3r.

First layer extrusion width: Extrusion (road) width of all first layer roads.

Perimeter extrusion width: Extrusion (road) width of perimeters.

Overlap: Percentage of road width to overlap between infill and perimeters and between adjacent perimeter roads. Default value set to 15%.

The remaining testing and printing were conducting using the LulzBot Taz 4 with a 0.75 mm nozzle. It was determined from previous testing that fewer print roads could be achieved if the road width was larger, subsequently reducing the required number of roads for an equivalent wall thickness and therefore reducing the print time. Another benefit of the larger nozzle is that the increased road width allows for the ability to have increased overlap between roads, thereby increasing bonding potential and decreasing the probability for separation of roads for any given layer. Although a 0.75 mm nozzle is considered "course", surface finish was not a requirement for the PHX. The MakerBot Z18 printer used for the triangular coupon testing could not be modified for use with a larger nozzle tip or the utilization of the software Slic3r for more control of the temperature/material flow/tool path of the print head. Although a larger nozzle will reduce part resolution, for purposes of this part the benefit of increased overlap between print roads and decreased print time support the goals of waterproofing and time efficient printing.

Moving forward with the Lulzbot Taz 4, the hexagon geometry was then patterned into a hexagon ring, all the while using the knowledge of FFF limitations/advantages to maintain relatively fast print times by alleviating infill in the walls of the PHX. To do so, vertical shell perimeters was set to the default value of 2. For 1.5 mm walls with 0.75 mm extrusion width, a.k.a. road width, there are two vertical perimeters per wall. Hence why two perimeters are necessary to

print each wall with two roads and therefore not require infill. Infill comes at a high cost of time and by creating a CAD that enables the printer to print each layer with two print roads per wall (i.e. 1.5 mm walls) will significantly reduce the time to print. Using Slic3r with the 0.75 mm nozzle, the overlap between adjacent print roads can be selected unlike MakerBot's proprietary software. The perimeter overlap was set to 15%, allowing for increased bonding potential between print roads of the same wall/layer and minimizing print defects that could result in part leakage. The default extrusion width, first layer extrusion width, and perimeter extrusion width were set to the nozzle diameter value of 0.75 mm to insure two perimeters were extruded for each wall. The hexagon patterned surface/cross section was then built vertically in what will be referred to as a prism design that allows for spacing between the hexagon columns as dictated by the previous calculations (see figure 3). To provide an average spacing of 1.3 cm for the full scale part, the necessary angle to taper the hexagon columns was found to be 15°. The 15° prism angle also allowed for enough overlap between layers for bonding to occur.

In order for water to fill the entire part via one inlet, the walls between adjacent hexagon columns needed to be raised slightly (3 cm). The height increase of exterior walls can be seen in figure 24. This not only allowed for fluid flow throughout the part but also a female end to which served as one half of the interlocking mechanism between components. The other half being a male tapered end extended 3 cm on to the top of the previously designed part.

Figure 24. Waterproof hexagon pattern with prism spacing test coupon (Full hexagon design.)

This hexagon patterned prism spaced design will be further referred to as the full hexagon design in reference to the hexagon pattern of 6 (figure 24). Speed settings for this coupon were left to default values. It was determined the intersection of the solid base and sides of the previous coupons was now a site of significant leakage. It appeared that the layer to layer adherence between the base and the first road was not sound potentially due to the 15° angle with respect to the z axis of the walls. To eliminate this problem and determine points of leakage on the walls of the part, a gasket and manifold clamped on both ends of an open ended part was introduced (see figure 25). After pumping ambient temperature water through the part, leaks developed at the apexes of the prism design as well as some of the faces. It is suspected that the cause of the apex regions leaking is that the slicing at this transition layer(s) did not allow for enough overlap between roads. This would create inadequate bonding and could lead to fracture or delamination at the regions. In order to select for increased overlap at these particular layers, significant editing of the G-code would be necessary as the Slic3r software does not allow for selective layer editing. Instead, thicker walls

were introduced to determine the effect of wall thickness on apex site leakage as well as face leakage.

Layer to layer separation was visibly the cause of the leaks on the faces. 3 mm walls (perimeters = 4) were attempted next and a nearly waterproof part off of the printer was achieved. Only two sites of leakage at the apexes of the prisms existed. Although this was a significant step forward in reducing part leakage, the print time doubled. Unable to print any faster than default values without increasing the number and severity of print defects, the 1.5mm wall thickness provided the necessary rigidity and acceptable print time but was unable to be waterproof off of the printer.
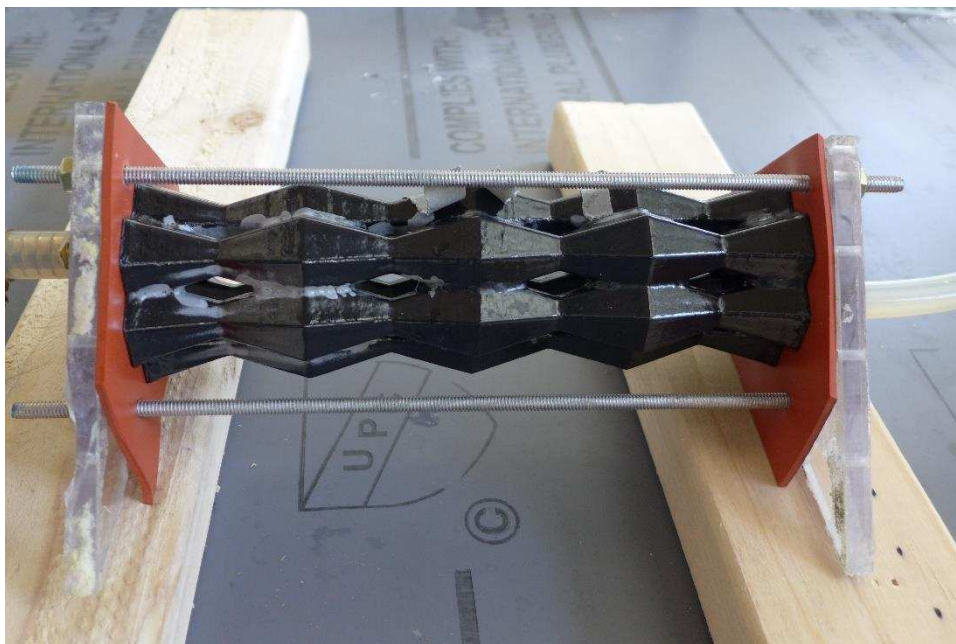
Figure 25. Waterproof full hexagon test coupon with TFAD post processing and gaskets on end. Tubing can be seen on the left and right of the PHX test unit, water flow rate through part is 1 L/min.

In order to reduce and/or eliminate the layer to layer separation observed, an insulated enclosure around the printer was constructed with a heat gun and temperature controller to control the printing environment. A heated build chamber reduces the temperature difference between the

49

molten extruding material and the surrounding air which then increases the bonding potential and reduces the delamination between layers.[9,24] Increasing the print environment temperature allows the print road to maintain a molten state longer since the time to cool and harden is also increased, subsequently increasing bonding. The temperature of the build chamber was set to 60°C. Test prints using the heated build chamber resulted in fewer regions of layer delamination, however it was obvious that an "off-the-printer" waterproof part with 1.5 mm walls was unachievable. Therefore, a post processing technique was developed to produce a waterproof part.

3.2 Thin Film ABS Deposition (TFAD) as a Post Processing   Technique
It is well known in the 3D printing community that acetone vapor deposition smooths and "polishes" parts.[38,39,40] Similarly, that acetone readily dissolves ABS and such a solution is often used to prep the printing surface for better build plate-part adherence to prevent warping.[41] When this is done, the acetone in solution evaporates, thereby depositing a thin layer of ABS on the build plate and allowing for better bonding between the build plate and the first layer of the part. Expanding on this concept, it was found that a solution of ABS and acetone would deposit a thin layer of ABS on all surfaces of the printed part after the part was quickly submersed in the solution and left to dry. When applied to the full hexagon test coupon with the manifold and gasket, this technique resulted in a water proof part at the maximum Sunchill^{TM} operating temperature for the PHX of 40°C at a flow rate of 1 L/min (figure 25). It appeared that the deposition of ABS in this manner fills and repairs the aforementioned print defects.

The optimum ABS-acetone deposition bath was found to be 1 kg ABS pellets to 4 gals of acetone. If the ABS concentration was too high, the part would dissolve as acetone trapped between the deposited layer and the part would begin to dissolve the part itself; leaving a wilted, warped product. If too little ABS was added, then very little plastic was deposited on the part

surface, thus needing to be submersed and dried repeatedly. After 4 submersions it was found that a part would begin degrading and dissolving at the ends, thereby reducing the dimensional accuracy of the part and subsequently preventing the successful mating between components. Depositing ABS on the parts surface using a 1kg ABS/4 gal acetone solution in three coatings giving a 24 hour drying time between the successive coatings yielded the ideal method for producing consistent waterproof parts that maintain dimensional accuracy for component mating. ABS deposition was capable of sealing layer to layer separations of ~0.5 cm. Any larger than 0.5 cm and ABS glue was necessary to successfully patch. Separations of this magnitude only existed on a few full size component prints.

TFAD Procedure for the Production of Waterproof 3D Printed Parts:

1. Determine necessary bath volume to submerse part. Dissolve required ABS in acetone to result in a concentration of 1 kg ABS/4 gal acetone and mix thoroughly until it is determined all ABS has dissolved.

2. Patch any layer-layer separations larger than 0.5cm with minimal amount of ABS glue.

3. Quickly submerse part in the ABS/Acetone solution and remove from bath. Rotate part on all axes until all excess solution drips off. This helps to avoid the solution from heavily coating in specific regions, particularly at the bottom of the part.

4. Hang dry for 12 hours.

5. Repeat steps 3 and 4 twice more.

The development of the TFAD technique allowed for the use of faster print speeds with 1.5 mm walls and resulted in shorter print time and the production of waterproof 3D printable parts capable of operating under the necessary conditions.
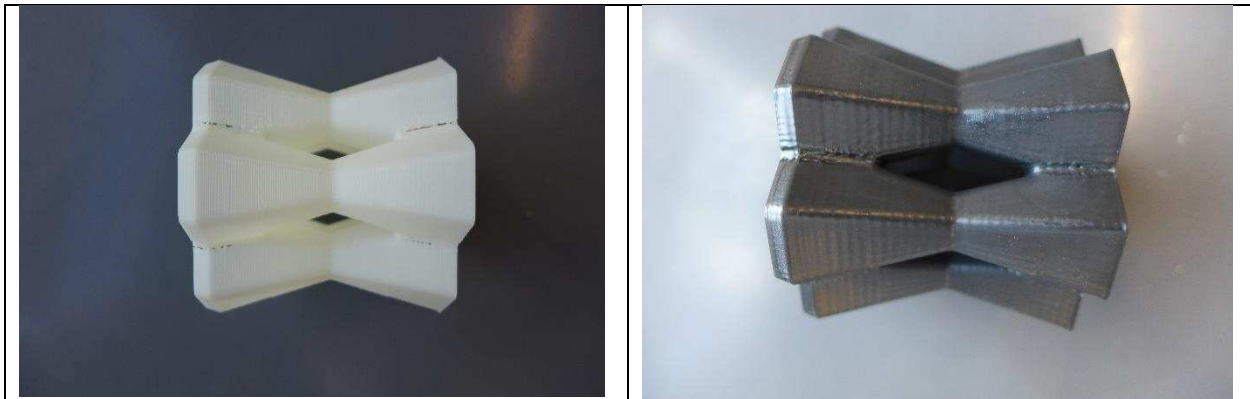
Figure 26. Untreated printed part (left). TFAD post processed part (right).

3.3 Full Scale Prototype Fabrication

Full Hexagon Design

After waterproof parts were successfully fabricated from printing and the post processing procedure with the small scale test coupons the parts were scaled up to the actual size of the CAD design of the full hexagon. The speed settings that allowed for the fastest print time vs print defects can be found in Table 5. Speed was increased to allow for faster printing but also due to the size of the part, acceleration/deceleration events are less of a concern. With smaller parts such as the test coupons, higher speeds can cause vibration in the print head due to the rapid acceleration and deceleration needed for corners, resulting in misaligned print roads. The TFAD post processing

Table 5. Print settings for full hexagon design.

Speed Parameter	Value
Perimeters	100 mm/s
External Perimeters	80 mm/s
Bridges	50 mm/s
First Layer Speed	60%

technique also allows for the increased print speed of the full scale part because minor print defects such as layer to layer separation, inherent to increased speeds, can easily be repaired.

After repeated attempts with the full hexagon design, it was found to not be waterproof after TFAD post processing. The exterior walls on the inside of the hexagon ring (figure 27) could not be accessed to patch with ABS glue and were observed to not be fully coated with ABS after the TFAD process. The crescent hexagon design was then introduced to combat these issues (figure 26).

The full hexagon design as seen in figure 28 consisted of 250mm long segments. Tapered male ends at the 15° prism angle were utilized as the method to interlock components. Any number of female-male segments can be used with a truncated female-female segment to yield a heat exchanger unit. The final PHX would comprise of an array of these units.

The test unit consisted of five of these parts (4 male and 1 female). ABS glue was applied to the male ends to join to the next segment. Male endcaps with a 2 mm thick base were printed to truncate and seal each end of the PHX unit. The infill density was set to 100% for these parts to insure waterproofness. It should be noted that the end cap components of the PHX are the only parts requiring infill for 3D printing. On the interior surface of this endcap a 1 cm thick, 2 cm diameter hexagon section was added to the CAD design of the end cap to provide enough material

for the tapping of a ¼" NPT to attach hose barbs to the endcaps. During the waterproof testing it was found that the PHX unit becomes difficult to handle due to weight. A reduction in the number of components was needed.
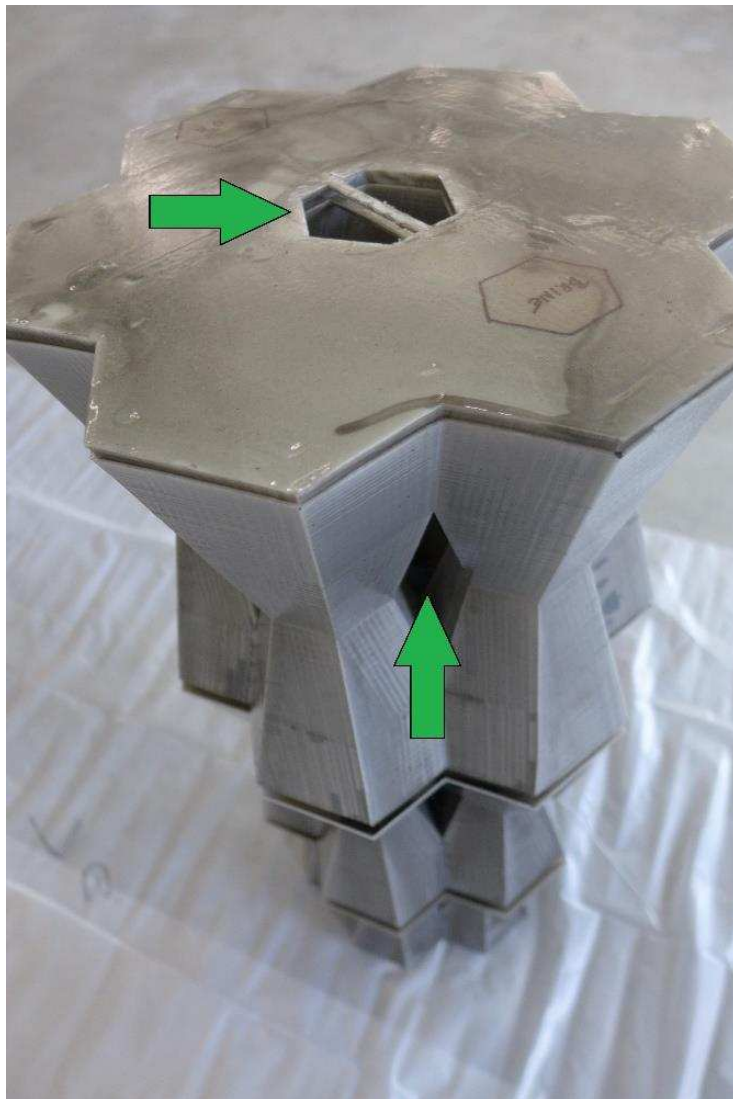
Figure 27. Full scale full hexagon design with TFAD post processing. The green arrows show the regions of inaccessibility to the inner hexagon surface where leakage was occurring.

Figure 28. Demonstration of TFAD technique of the full hexagon design and the size, shape, and number of components of the unit. The assembly of printed components prior to TFAD was rejected after this test as the amount of ABS solution required is far greater than TFAD of the individual components prior to assembly.

Crescent Design

The crescent design was introduced to prevent the leakage issues present in the full hexagon design figure 29. This design allowed for access to all faces that in the event that a leak was present it could easily be sealed with a light application of ABS glue. The crescent design is an evolution of the full hexagon design in that it is simply one half of that design comprised of three hexagon prism columns instead of a ring of six.

Figure 29. Crescent design with TFAD post processing and all hose barbs (printed and metal) installed.

To reduce weight and increase the ease of handling of the PHX unit once full of water, the test unit of the crescent design was comprised of two male, one female, and endcap parts. After post processing and assembly it was found that this design was waterproof.

Double Walled Crescent Design

It was quickly determined that the crescent design was waterproof. The next step was to incorporate the double wall feature described in the calculations sections. The double wall is necessary to cool the fresh water stream as well as separate this stream from the brine refrigerant. Initial design of the double wall feature was to mimic the contour of the outer wall at a 1 cm spacing from said outer wall (Figure 30). Separate prints would interlock in the same fashion as the single walled tests. It was found that the test unit consisting of 3 printed components (2 male, 1 female, and endcaps) was waterproof on the exterior, but was not waterproof between compartments (brine chamber and water chamber). The point of leakage was determined to be the connections at the interlocking sites. TFAD post processing appeared to mildly warp/distort the walls at the male ends of the parts causing an imperfect seal when parts were glued together. Less stress was imposed on the male ends (convex) if the parts were hung to dry after ABS deposition by their female ends (concave). This caused undried ABS solution to accumulate at the bottom, male end, and warp the part as the increased acetone concentration made the plastic more malleable. Being an interior wall, the double wall could not be repaired/patched with ABS as could be done to the exterior surface. Another approach to incorporate a double wall was necessary.
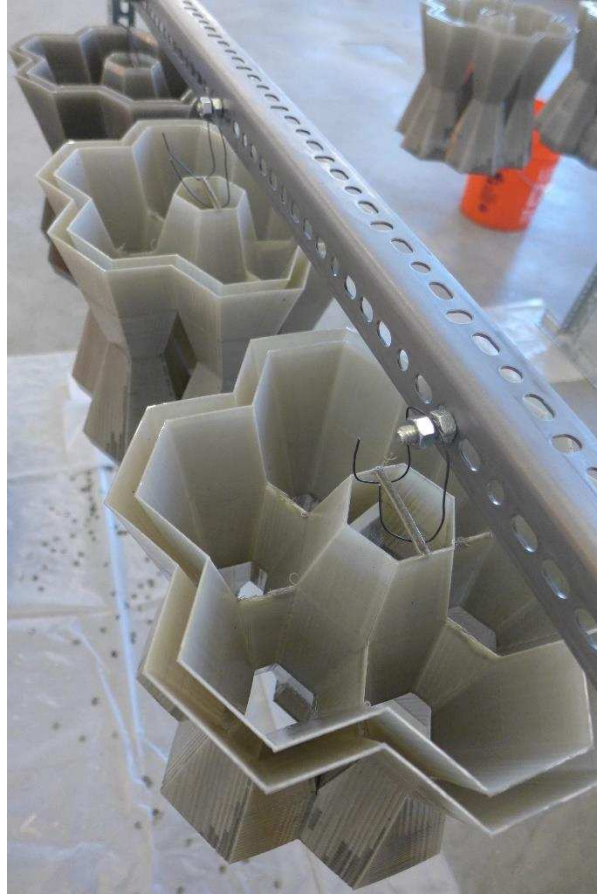
Figure 30. Full hexagon design demonstrating initial double wall design. Parts are hanging to dry after a TFAD coating.
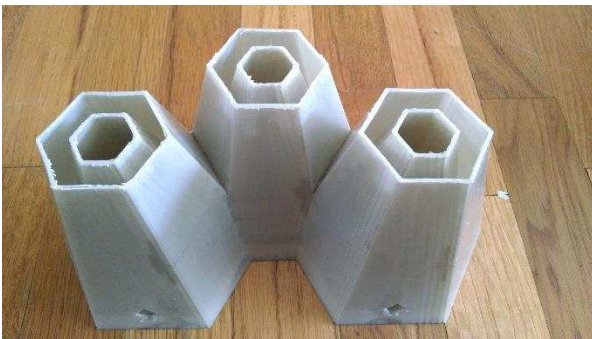
Figure 31. Cross section of self-contained double wall design in crescent part. The 1 cm gap for the water compartment can be seen at left. The double wall tapers to the outside wall at the end of the part, thus allowing parts to be interlocked as was done with the previous single walled tests (right).

To prevent leakage between compartments it was decided the outer water chamber should remain enclosed for each printed part and thus interlocking of parts could be accomplished in the same manner as the single walled tests. In order to flow water between parts, hose barbs could be installed on the exterior surface and connected by small lengths of flexible tubing. A cross section of a crescent part with the described double wall design is shown in figure 31.

Two male, one female, endcaps, and water chamber hose barbs were printed, post processed, and assembled to achieve a fully waterproof (to exterior and between compartments) PHX unit. The final design of a single unit of the PHX can be seen in figure 29. The complete list of print settings used to print the final prototype of the PHX are listed in the appendix.

4   Experimental Testing

In order to evaluate the accuracy of the assumptions made in the previously described calculations

of the PHX, an experimental test rig was constructed. The experimental testing apparatus can be

seen in figure 32.
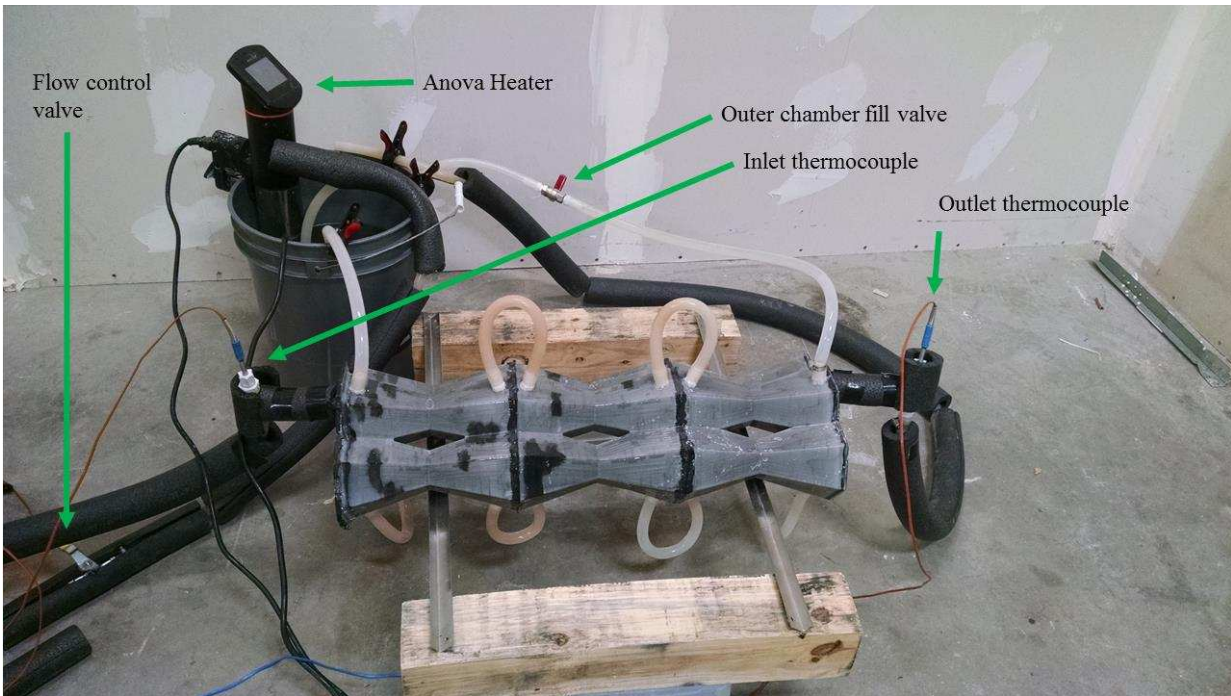
Figure 32. Test rig for determination of heat transfer performance of the final PHX design (crescent double wall).

4.1 Experimental Setup

An Anova Sous Vide Immersion Circulator was used to maintain a constant bath temperature of

40°C. A standard 5 gallon bucket was used as the container for this bath. A sump pump placed at

the bottom of this bucket was used to flow water through the inner "brine" chamber of the PHX.

A valve and flow meter were inserted prior to the inlet of the PHX. The volumetric flow

rate was set to a low flow rate of 45 ccm to allow for a greater temperature difference between the

inlet and outlet and subsequently, reduce systematic error in temperature measurements. To

monitor temperatures, three T-type thermocouples were used. The first thermocouple was inserted

immediately prior to the inlet. The second thermocouple was inserted immediately after the outlet. The third thermocouple was used to monitor the ambient temperature. It was placed a distance away from the PHX and suspended above the ground at the same height as the PHX to minimize effects of PHX heat dissipation and temperature gradients respectively. Inlet and outlet hoses where insulated with standard pipe insulation.

The outer "water" chamber of the PHX was filled with ambient temperature water and rotated on end to allow all air in this chamber to escape. No leakage to the floor or the inner chamber was observed.

The inner chamber of the PHX was filled next with 40°C water from the heated bath. The PHX was again rotated, allowing all air to escape this chamber. Careful attention was observed to not allow any water in the outer chamber to escape during this procedure. A valve was installed on the outer chamber hose nearest the inlet side of the PHX and closed to prevent any water from escaping this chamber while removing air from the central chamber.

The setup was placed in a space with three surrounding walls opening to a large warehouse space. To prevent air flow into this space, porous air neutralizing sheets were hung from the ceiling to the floor, effectively "enclosing" the testing space and preventing any wind currents inside the testing area.

The thermocouples were connected to a National Instruments cDAQ-9174 NI compact DAQ module and read by a previously written GUI in Eclipse.

Temperature measurements were taken every 100s and each measurement was the average of 10 reads over an interval of 8 hours to allow the system to come to steady state.

4.2 Results

The data over the steady state region of the 8 hour collection period is shown figure 33. Averaging the temperatures of the inlet, outlet, and ambient thermocouples over this region the temperatures are 36.21°C, 28.93°C, and 13.95°C respectively. Converting the volumetric flow rate of 45 ccm to a mass flow rate, it was found to be 0.00075 kg/s. The average heat removed from the PHX was determined to be 22.84 W.
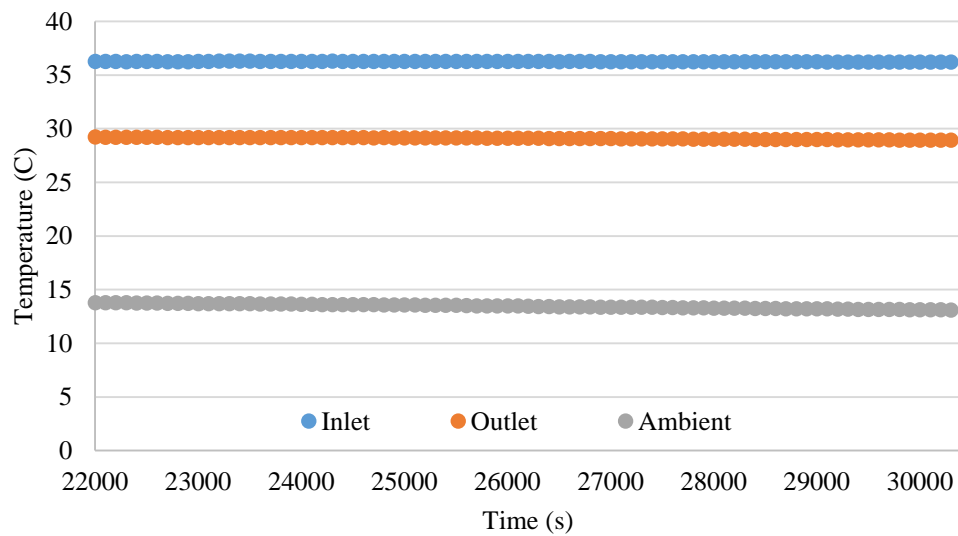
Figure 33. Steady state temperatures of the inlet thermocouple (blue), outlet thermocouple (orange), and the ambient thermocouple (grey).

4.3 Discussion

In order to compare the previously described EES model of the overall system to the experimental results, minor modifications were made. The modeling of the brine chamber was altered to be internal pipe flow with flow rate 0.00075 kg/s and T_brine was taken to be the log-average of the inlet and outlet temperatures. In order to determine q, the surface area of the PHX unit being tested was specified. This area was 0.471 m², determined from the CAD model. The flat plate air model was replaced with a horizontal pipe correlation with diameter equal to the average

hexagon diameter of the PHX (7.56 cm). The results of making these modifications to the PHX

model can be seen in table 6.

Table 6. Results of heat
transfer calculations modified
to model experimental testing
environment and fluid flow.

q	29.61 W
h_brine	110 W/m^{2}K
h_water	147.7 W/m^{2}K
h_air	4.112 W/m^{2}K
R_brine	0.01925 K/W
R_water	0.01437 K/W
R_air	0.5163 K/W
R_total	0.5853 K/W
Tp1	30.71°C
Tp2	30.19°C
Tp3	29.76°C
Tp4	29.24°C

The result of 29.61 W is a 26% error from the experimentally determined q. It is clear the

model is overestimating the heat transfer of the PHX given the experimental conditions. One

possible explanation for this is there is not a correlation to accurately describe the complex

geometry inherent to the PHX. Choosing the horizontal pipe correlation to model the heat transfer

to the air assumes a constant diameter along the pipe with the specified area. However, in reality

the diameter of the PHX varies along its length. There are gaps between pipes due to the prism

design where the diameter is small and at the ends the gap between pipes does not exist. At the

ends of the PHX it effectively becomes one "solid" part, thereby decreasing the effective surface area for heat transfer and subsequently the observed q.

Making the modification to the air model of a horizontal cylinder with diameter of 7.56 cm in the overall PHX model used in the calculations section, the required area increases from the previously determined 20.46 m^2 to 21.35 m^2. The heat transfer coefficient for air for this model was slightly reduced to 3.75 W/m^2-K. Although there is a discrepancy between the q determined from the model and the experimentally observed q, the surface area for the overall PHX model remains relatively the same regardless of the updated air model. This is attributed to the similarity between the heat transfer coefficients for the air found from the initial calculations and the experimental model, thereby not significantly affecting the total surface area requirement of the PHX.

4.4 Precipitation Testing

Large scale precipitation testing of $Na_2CO_3 \cdot 10H_2O$ was conducted using a six foot section of a 3" clear acrylic pipe in order to determine crystal formation and ease of solvation at this scale. The transparent nature of this pipe would allow for the observation of crystal size and growth dynamics. A 5 gallon tank was used to prepare the stock solution to be injected into the pipe. Three gallons of water were heated to 30°C and sodium carbonate was added until a saturated solution was reached (30% m/m). The warm brine solution was then poured into the 3" acrylic pipe and left to come to room temperature (20°C).

After an 8 hour period significant crystal growth was observed (figures 34-35). It was found that the crystal formation filled 60% of the volume of the pipe. No crystals were observed to have grown on the upper surface of the interior of the pipe. This signals that crystallization occurred in solution and settled to the bottom of the pipe rather than nucleating on the interior pipe surface.

The saturated solution remaining in the upper cavity of the pipe was decanted and it was revealed that the crystal growth in the pipe had fused into one solid structure.
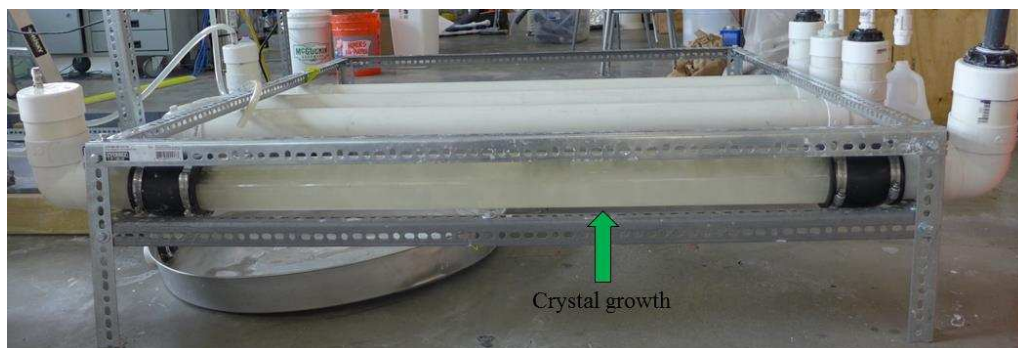
Figure 34. Large scale $Na_2CO_3 \cdot 10H_2O$ precipitation testing in a 3" clear acrylic pipe. Crystal growth was observed to fill 60% of the volume of the pipe.

To test the ease of solvation, fresh water was pumped into the cavity of the pipe at a flow rate of 1 L/min. Samples were taken from the outlet stream and subsequent density measurements

Figure 35. Enhanced view of $Na_2CO_3 \cdot 10H_2O$ crystal growth in pipe**.**

revealed very little salt was being solvated. It was suspected that this was due to the small surface area contact the water had with the crystals. Solvation of the $Na_2CO_3 \cdot 10H_2O$ would cause an

increase in density until saturation occurred and therefore remain on the surface of the bulk crystal until exiting at the outlet. To confirm this suspicion, green food dye was injected at the inlet of the pipe to track the fresh water path. Color was observed in the top 1/3 of the volume of the pipe with a thin layer of saturated opaque solution between the colored water stream and the bulk crystal, verifying the previous hypothesis. After 4 hours of continuous fresh water flow, it appeared that little to no solvation occurred and the large $Na_2CO_3 \cdot 10H_2O$ crystal structure in the bottom 60% of the pipe still remained. Nucleation on the walls of the PHX would be necessary to aid in providing increased surface area to more efficiently solvate the $Na_2CO_3 \cdot 10H_2O$. Various surface treatments of the interior of printed test coupons were investigated.

4.5 Surface Treatment Testing

To determine if crystal growth of $Na_2CO_3 \cdot 10H_2O$ could be stimulated on the walls and ceiling of the brine chamber of the PHX in order to enhance solvation, test coupons with viewing windows were printed and various surface treatments were applied to their interiors. Hexagon pipe coupons with 1 cm sides and 1.5 mm walls were fabricated with one open end and post processed using the TFAD technique to closely mimic the surface of the full scale PHX unit.

The interior of each coupon was then altered after TFAD processing. Coupon A was left as a control; no addition surface treatment beyond TFAD was applied. Sodium carbonate powder was embedded into the interior surface of coupon B immediately after the TFAD to determine if the embedded crystals would act as a seed site for nucleation. Addition of a saturated solution of sodium carbonate was hoped to prevent solvation of the embedded crystals. A material insoluble in water with a crystal structure identical to that of $Na_2CO_3 \cdot 10H_2O$ was sought to remedy the potential of dissolution, however no material with said properties was found. Coupon C was scored with 220 fine grit sand paper. One swipe per interior face was applied to coupons C-E in order to normalize scoring between coupons. Coupon D was scored with 150 medium grit sandpaper.

Coupon E was scored with 60 course grit sandpaper. Fine pea gravel was attached to the interior surface of coupon F immediately following TFAD to determine if such a rough textured surface would promote nucleation and/or act as seed sites for crystal growth. After surface treatments were applied a clear acrylic slide was glued to the open end of each coupon to observe the formation of $Na_2CO_3 \cdot 10H_2O$ crystals and labeled to differentiate between surface treatments.

A hole was drilled at the top of each coupon and each coupon was then injected with saturated 30°C sodium carbonate solution. A small amount of ABS glue was applied to each injection hole to seal the coupon. The coupon were then left to precipitate over an 8 hour period. The observed crystal growth during this time was identical to that of the large scale 3" clear acrylic pipe precipitation test. All coupons had crystals that filled the bottom 50-60% of their volumes (figure 36). No crystals were observed to form on the walls or ceilings of the coupons. This indicates that the precipitation of $Na_2CO_3 \cdot 10H_2O$ occurs in solution and upon formation the increased density of the crystal causes it to fall to the bottom of the container. Further crystal growth can then occur at these sites, resulting in the large bulk crystal formation in the 3" clear acrylic pipe and surface treatment tests. The natural convection heat transfer in these systems cools the saturated 30°C sodium carbonate solution slowly, resulting in the large crystals observed. In order to reduce the size of the crystals and prevent the formation of a large solid in the bottom of future testing containers it is proposed that agitation of the solution via auger or other method in order to disrupt the aggregation of crystals and subsequently maintain a slurry of small crystals for ease of solvation.
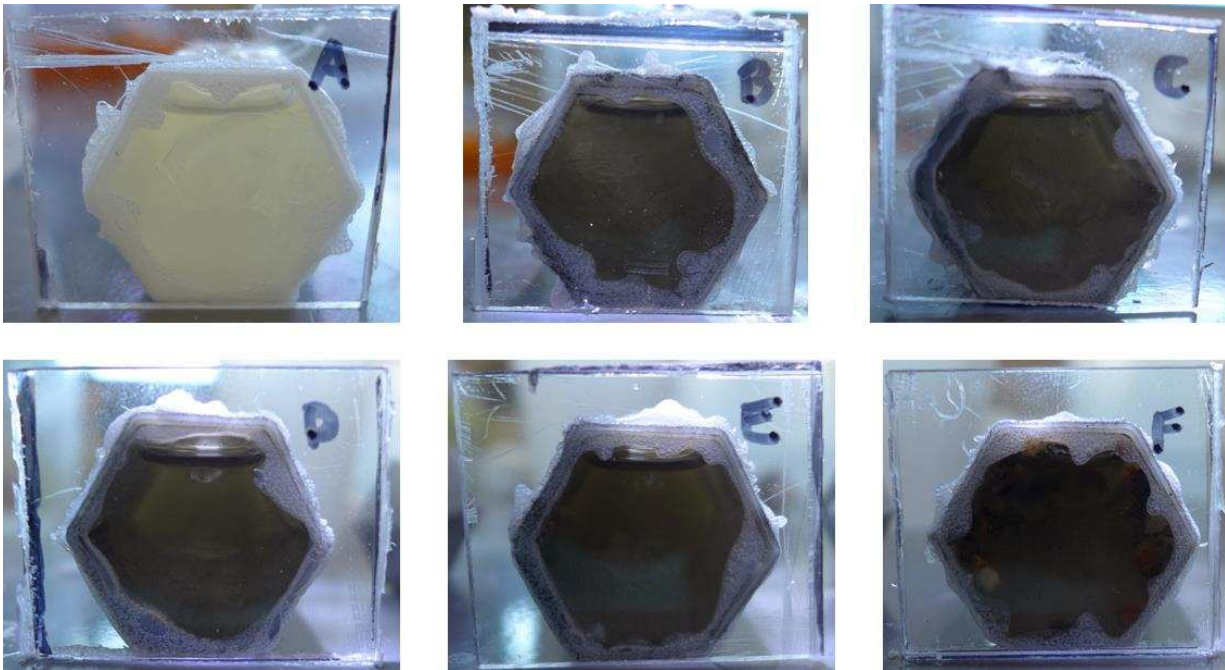
Figure 36. Surface treatment testing of printed hexagon test coupons. A: Control, B: Embedded Na3CO3 powder, C: 220 grit sandpaper scoring, D: 150 grit sandpaper scoring, E: 60 grit sandpaper scoring, F: Embedded fine pea gravel.

Slurry formation testing was conducting in a 5 gallon tank by filling with 3 gallons of 30°C saturated sodium carbonate solution and agitating with a paddle stirrer powered by a corded drill. The 5 gallon tank was sealed with a lid that allowed the drive shaft of the paddle stirrer to pass through. Agitation was continued until the temperature of the solution reached 1-2°C above ambient and significant crystal growth was observed (~ 1 hour). This test verified the previous hypothesis. A slurry was generated as the crystal size was significantly reduced and suspended in solution. The act of agitation significantly increases the heat transfer rate via the increased convection in the brine solution and subsequently the increased cooling rate results in smaller crystal size. An additional gallon of ambient temperature water was added to the tank and stirred at a low rate to solvate the $Na_2CO_3 \cdot 10H_2O$. In 5 minutes a temperature of 10°C was achieved and all $Na_2CO_3 \cdot 10H_2O$ was solvated. The formation of a slurry via agitation demonstrates the necessity of such a technique in order to effectively solvate the precipitated $Na_2CO_3 \cdot 10H_2O$. An auger placed

in each hexagon pipe of the PHX design was proposed, significantly increasing the complexity of constructing a full size system. Before such a design consideration could be implemented the air-gap membrane unit produced by the Fraunhofer Institute failed. Tears in the wound fabric of the device due to the high osmotic pressure at increased concentrations of sodium carbonate solutions were the source of failure. Without an alternative for this unit coupled with the potential design complexity of $Na_2CO_3 \cdot 10H_2O$ precipitation and length of time necessary for the fabrication of the PHX, this prototype of Sunchill^{TM} was abandoned and new prototypes involving different methods for concentration/separation were developed.

5   Conclusions and Future Work

The required surface of the PHX needed was 21 m^2. The area of the unit used for experimental testing was 0.471 m^2. In order to achieve the total required surface area, 43 of these units would be needed. The total print time required to produce this single unit was approximately 45 hours. Each of the "body" components (2 male, 1 female) of the PHX required 12 hours to print and the two endcaps printed together took 9 hours to print. This does not include the 3 days of post processing time. Using the print time alone, it would take 80 days of continuous printing to complete the unit. When the allotted time for installation, testing, and modification to the refrigeration system in Mozambique was 6 months (180 days), printing alone would require 44% of that time to produce one component of the refrigeration system. This is unreasonable. Although the PHX described here is one of two known examples of a documented 3D printable, waterproof heat exchanger, it is not a feasible option for use with the Rebound Sunchill^{TM} system. However, the TFAD post processing waterproofing technique developed during this project could be applied to other technologies utilizing fused filament fabrication where time constraints are less intrusive to product development but waterproofing is necessary.

In light of the failure of 3D printing to deliver a full PHX in an acceptable time, it is clear that such additive manufacturing technology needs advancement. Alternatives to the fused filament fabrication method used for this work such as stereolithography (SLA) could offer benefits in terms of print time but have since been expensive. One of the latest advancements in SLA methods, the Carbon3D system using continuous liquid interface production (CLIP) is capable of producing parts in extremely short times. A print that would take 11.5 hours on a standard SLA machine could now be printed using CLIP on Carbon3D in 6.5 minutes. This technology is exciting in its ability to produce high resolution parts in a relatively short time and be cost effective, but advancements such as this are still limited to the use of photopolymers that

degrade over time, becoming brittle and fracture prone in as little as one year. In order for 3D printing to become a viable commercial manufacturing technique for polymer heat exchangers advancements need to be made in the material curing and photochemistry properties of the polymer resins.

References

[1] Critoph, R. An Ammonia Carbon Solar Refrigerator For Vaccine Cooling. *Renew Energy*, 5 (1994) 502–508.

[2] El Fadar, A. Mimet, A. Perez-Garcia M. Study of An Adsoprtion Refrigeration System Powered by Parabolic Trough Collector and Coupled with a Heat Pipe. *Renew Energy*, 34 (2009). 2271-2279.

[3] Fernandes, M. Brites, G. Costa, J. Gaspar, A. Costa, V. Review and Future Trends of Solar Adsorption Refrigeration Systems. *Renewable and Sustainable Energy Reviews*, 39 (2014) 102-123.

[4] Fan, Y. Luo, L. Souyri, B. Review of Solar Sorption Refrigeration Technologies: Development and Applications. *Renewable and Sustainable Energy Reviews*, 11 (2007) 1758-1775.

[5] Anyanwu, E. Review of Solid Adsorption Solar Refrigerator I: An Overview of the Refrigeration Cycle. *Energy Conversion and Management*, 44 (2003) 301-312.

[6] Bengtson, H. Stonecypher, L. Double Pipe Heat Exchanger Design. www.brighthubengineering.com. (2010).

[7] Cengel, Y. Heat Transfer: A Practical Approach 2nd Edition. New York: McGraw-Hill. (2002) 667-704.

[8] Incropera, F. P., Dewitt, D. P., Bergman, T. L., Lavine, A. S. Fundamentals of Heat and Mass Transfer 6th Edition. New York: John Wiley and Sons (2007).

[9] Gibson, I., Rosen, D. W., Stucker, B. Additive Manufacturing Technologies: Rapid Prototyping to Direct Digital Manufacturing. New York: Springer Science (2010).

[10] Dupont, "Flexible Plastic Tube Bundle and Method of Making", US3315740 A (1967).

[11] Schweitzer, P. A., Mechanical and Corrosion-Resistant Properties of Plastics and Elastomers. New York: Marcel Dekker (2000).

[12] Tasker, S., Chambers, R. D., Badyai, J. P. S., Surface Defluorination of PTFE by Sodium Atoms. *J. Phys. Chem.* 98 (1994) 12332-12446.

[13] Tanaike, O., Yoshizawa, N, Hatori, H., Yamada, Y. Porous Carbons Derived From PTFE Defluorinated with Alkali Metals. *Fuel Chemistry Division Preprints,* 47 (2002) 468-469.

[14] Githens, R. E., Minor, W. R. and Tomsic, V. J. Flexible-tube heat exchangers. *Chemical Engineering Progress*, 61 (1965) 55-62.

[15] Mannoni, A., Vitali, D., Development of All-Nylon Charge Air Cooler for Automotive Applications, *Vehicle Thermal Management: Heat Exchangers and Climate Control*, Nashville, TN (2001).

[16] Zaheed, L., Jachuck, R. J. J., Review of Polymer Compact Heat Exchangers with Special Emphasis on a Polymer Film Unit. *Applied Thermal Engineering*, 24 (2004) 2323-2358.

[17] Chen, L., Li, Z., Guo, Z.-Y. Experimental investigation of plastic finned-tube heat exchangers, with emphasis on material thermal conductivity. *Experimental Thermal and Fluid Science*, 33 (2009) 922-928.

[18] Cervallos, J. G., Thermal and Manufacturing Design of Polymer Composite Heat Exchangers, PhD dissertation, University of Maryland, 2004.

[19] Wohlers, T.T., *Wohlers Report 2011: Additive Manufacturing and 3D Printing State of the Industry Annual Worldwide Progress Report*, Wohlers Associates, Inc., Fort Collins, CO (2011).

[20] Stratasys Inc. ABS. 2007.

[21] Bellini, A., Güçeri, S. and Bertoldi, M. Liquefier dynamics in fused deposition, *Journal of Manufacturing Science and Engineering, Transactions of the ASME*, 126 (2004) 237-246.

[22] Venkataraman, N., Rangarajan, S., Matthewson, M.J., Safari, A., Danforth, S.C. and Yardimci, A. Mechanical and rheological properties of feedstock material for fused deposition of ceramics and metals (FDC and FDMet) and their relationship to process performance. *Solid Freeform Fabrication Proceedings*. University of Texas (1999).

[23] Venkataraman, N., Rangarajan, S., Matthewson, M.J., Harper, B., Safari, A., Danforth, S.C., Wu, G., Langrana, N., Guceri, S. and Yardimci, A. Feedstock material property-process relationships in fuseddeposition of ceramics (FDC). *Rapid Prototyping Journal* 6 (2000) 244-252.

[24] Turner, B. N., Strong, R., Gold, S. A. A Review of Melt Extrusion Additive Manufacturing Processes: I. Process Design and Modeling. University of Dayton, Ohio (2014).

[25] Bellini, A. Fused deposition of ceramics: a comprehensive experimental, analytical and computational study of material behavior, fabrication process and equipment design, PhD dissertation, Drexel University, Philadelphia, PA (2002)

[26] General Chemical Industrial Products. Soda Ash: Technical and Handling Guide. Green River, WY.

[27] Powell, R. W., Ho, C. Y., Liley, P. E. Thermal Conductivity of Selected Materials. *National Standard Reference Data Series-National Bureau of Standards* 8 (1966).

[28] Kraus, A. D., Aziz, A., Welty, J. Extended Surface Heat Transfer. New York: John Wiley and Sons. (2002) 381.

[29] Nellis, G. Klein, S. Heat Transfer. New York: Cambridge University Press. (2008) 689-672.

[30] Shah, R. K., London, A. L. Laminar Flow Forced Convection in Ducts. Academic Press, New York (1978).

[31] L. Zaidi, M. Kaci, S. Bruzaud, A. Bourmaud, Y. Grohens, Effect of Natural Weather on the Structure and Properties of Polylactide/Cloisite 30B Nanocomposites. *Polymer Degradation and Stability* 95 (2010) 1751-1758.

[32] S. Dadbin, F. Naimian, A. Akhavan, Poly (lactic acid)/Layered Silicate Nanocomposite Films: Morphology, Mechanical Properties, and Effects of γ-Radiation. *Journal of Applied Polymer Science* 122 (2011) 142-149.

[33] S. Bocchini, K. Fukushima, A.D. Blasio, A. Fina, A. Frache, F. Geobaldo, Polylactic Acid and Polylactic Acid-Based Nanocomposite Photooxidation, Biomacromolecules 11 (2010) 2919-1926.

[34] Martin, O. Averous, L. Polylactic Acid: plasticization and Properties of Biodegradable Multiphase Systems. *Polymer* 42 (2001) 6209-6219.

[35] Tiganis, B. E., Burn, L. S., Davis, P., Hill, A. J. Thermal Degradation of Acrylonitrile-butadiene-styrene (ABS) blends. *Polymer Degradation and Stability* 76 (2002) 425-434.

[36] Sodegard, A. Mikael, S. Properties of Lactic Acid Based Polymers and Their Correlation with Composition. *Progress in Polymer Science* 27 (2002) 1123-1163.

[37] Hodgson, G., Ranellucci, A., Moe, J. Slic3r Manual. Aleph Objects Inc. (2016).

[38] Chapman, B. Desai, S. Muraoka, M. Vidolova, T. Investegating Methods of Prototyping with ABS. Olin College of Engineering, Needham, MA. (2014).

[39] Horvath, J. Mastering 3D Printing. New York: Apress. (2014) 129-135.

[40] Kraft, C. Smoothing Out Your 3D Prints with Acetone Vapor. www.makezine.com. (2014).

[41] Landry, T. ABS Bed Adhesion Tips and Tricks. www.matterhackers.com. (2014).

Appendix

Summary of Print Settings

Layer height	0.325
First layer height	100%
Perimeters	4
Spiral vase	Unchecked
Solid layers (top)	3
Solid layers (bottom)	3
Extra perimeters if needed	unchecked
Avoid crossing perimeters	unchecked
Detect thin walls	Checked
Detect bridging perimeters	Checked
Seam position	aligned
External perimeters first	Checked
Fill density	100%
Fill pattern	Rectilinear
Top/bottom fill pattern	Rectilinear
Combine infill every	1 layers
Only infill where needed	unchecked
Solid infill every	0 layers
Fill angle	45 degrees
Solid infill threshold area	70 mm2
Only retract when crossing perimeters	unchecked
Infill before perimeters	unchecked
Loops (minimum)	2
Distance from object	6 mm
Skirt height	1 layers
Minimum extrusion length	0 mm
Brim width	0 mm
Generate support material	unchecked
Raft layers	0 layers
Perimeters	100 mm/s
Small perimeters	60%
External perimeters	80%
Infill	50 mm/s
Solid infill	50%
Top solid infill	100%
Support material	100 mm/s
Bridges	50 mm/s
Gap fill	60 mm/s
Travel	130 mm/s
First layer speed	60%
Acceleration: Perimeters	3500 mm/s2
Acceleration: Infill	4200 mm/s2

Acceleration: Bridges	3500 mm/s2
Acceleration: First Layer	0 mm/s2
Acceleration: Default	3500 mm/s2
Default extrusion width	0.75 mm
First layer width	0.75 mm
Perimeters width	0.75 mm
External perimeters width	0
Infill width	0
Solid infill width	0
Top solid infill width	0
Infill/perimeter overlap	15%
Bridge flow ratio	1
XY size compensation	0 mm
Threads	2
Resolution	0.02 mm
Filament diameter	2.88 mm
Extrusion multiplier	1
Extruder temperature (first layer)	230°C
Extruder temperature (other layers)	230°C
Bed temperature	0
Nozzle diameter	0.75 mm